

**NASA
Technical
Paper
1983**

May 1982

Application of Modal Control to Wing-Flutter Suppression

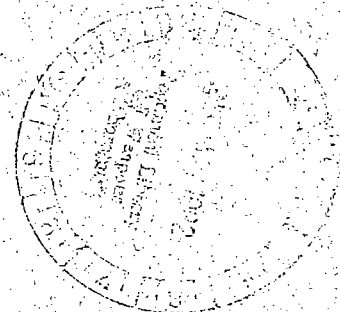
Aaron J. Ostroff
and Samuel Pines

NASA
TP
1983
c.1

TECH LIBRARY KAFB, NM
0068139

LOAN COPY: RETURN TO
NASA TECHNICAL LIBRARY
WRIGHT-PATTERSON AFB, OH

NASA



**NASA
Technical
Paper
1983**

1982

TECH LIBRARY KAFB, NM



0068139

Application of Modal Control to Wing-Flutter Suppression

Aaron J. Ostroff
*Langley Research Center
Hampton, Virginia*

Samuel Pines
*Analytical Mechanics Associates, Inc.
Jericho, New York*

NASA

National Aeronautics
and Space Administration

Scientific and Technical
Information Branch

SUMMARY

This paper describes a discrete modal-control design approach that is applied to a single-control-surface, unswept aircraft wing subject to bending-torsion flutter. The modal approach is a mathematical method to decouple the equations of motion into isolated differential equations. In this paper, a pole-placement approach is then applied to determine stability gains in the discrete plane using only the two complex-conjugate flutter-mode equations. A fixed-gain Kalman filter is used to estimate the modal amplitudes using three measurements. Results are presented for a full-state estimator (36 states) and two reduced-state estimators using two different closed-loop pole locations. The control law is designed for a dynamic pressure that is 50 percent greater than the uncontrolled-flutter dynamic pressure. With constant control-law gains, the closed-loop system remains stable over the dynamic-pressure range from flutter onset to approximately an 80-percent increase in pressure.

INTRODUCTION

In the 1960's and early 1970's, research in controlling the primary mirror of a large orbiting space telescope was conducted. The goal was to control the figure error of the primary mirror to a fraction of a wavelength with many actuators mounted at the rear of the mirror and with a figure-error sensor located at the center of curvature. A modal-control technique was developed (ref. 1) to decouple the equations of motion representing the plant. The technique allowed each controlled mode to be individually compensated for in the modal domain. Additional research applying the modal-control approach to the mirror problem is described in references 2 and 3. Subsequent to this work there has been renewed interest in applying modal control to other areas, particularly to the area related to large, flexible spacecraft control (refs. 4 to 7). Another area in which modal control could have a significant impact relates to flutter suppression. This paper describes a discrete modal-control design approach that is applied to a single-control-surface, unswept aircraft wing subject to bending-torsion flutter. One advantage of the modal-control approach is that the flutter mode, as well as all other flexible-wing modes, can be mathematically represented by two isolated complex-conjugate equations. The decoupled nature of the modal-control approach allows additional insight into the control problem, and it is possible to use either classical control techniques or modern control theory to design feedback gains. In this paper, a pole-placement approach is used to calculate the stability feedback gains, which are analytically designed by using only two complex-conjugate flutter-mode equations.

Several other approaches have been applied to the flutter-suppression problem. These approaches include an aerodynamic energy method (refs. 8 and 9) and optimal-control approaches (refs. 10 to 12). A modal-control analysis is used in reference 12, but the design is for a continuous-control law and the performance index is expressed in terms of a quadratic cost function that is related to all of the modal amplitudes. As described above, the main thrust of this paper is to isolate and control only the flutter mode, influencing the higher order modes as little as possible. The modal-control approach appears to be a good method to meet this goal.

The first section of this paper includes a brief description of the wing and the various subsystems that comprise the open-loop plant. Detailed models of all subsystems are given in appendix A.

The second section includes the equations for transforming the physical domain to the modal domain and includes the form of the various matrices. A theoretical solution for the modal equations of motion is presented for a discrete sampling period. The analysis carries through to the use of the flutter-mode equation to design the stability feedback gains.

While the research was being conducted, it became obvious that wind gust and the external disturbance states should be estimated. The approach used in the third section is to augment the modal equations and solve a convolution integral to determine the effect of these states on the modal amplitudes. The discrete form for the total system with 36 state equations is shown.

The fourth section of this paper shows how the discretized fixed-gain Kalman filter is calculated. The symbology illustrates the matrices that are to be approximated both for off-design analysis and for reduced-state estimation. Two methods are presented for calculating the reduced-state estimator. Also included are the equations to calculate the estimator closed-loop stability and the total closed-loop-system stability.

The fifth section ("Results") contains several figures showing the performance for two design eigenvalue locations. One eigenvalue has a low damping ratio of 0.14 and the other a higher damping ratio of 0.62. Performance is determined by normalizing the root-mean-square (rms) value of each variable about a zero mean with the rms value of wind gust about a zero mean. The plots shown compare a base run using perfect modal feedback and stability gains adjusted for each dynamic pressure with several runs using three output measurements with an estimator. Both full-state estimation and reduced-state estimation runs are presented. The "Results" section also contains figures showing some typical data signals for several states and step responses due to an external command input.

DESCRIPTION OF MODEL

An unswept aircraft wing (fig. 1) subject to bending-torsion flutter was used as a model for application of the modal-control concepts. Most of the data for this wing are in reference 13. The semispan for this wing model is 5.08 m (200 in.) and the chord varies linearly from 2.54 m (100 in.) at the root to 1.52 m (60 in.) at the tip. Five grid points, excluding the root section, are located along the elastic axis at the corresponding 40-percent-chord location. The aerodynamic center is located at 25 percent chord.

The wing model has the capability of incorporating one or more control surfaces along either the leading or the trailing edge or along both edges. For all analyses in this paper, a single trailing-edge control surface is used. The equations of motion that describe the complete system are derived from several detailed models described and defined in appendix A. These detailed models include the structural equations of motion, unsteady aerodynamics with Jones' approximation of the Wagner function (refs. 14 and 15), an external-disturbance model using the Küssner function (ref. 16) to relate the wind gust to forces and moments on the wing, a Dryden wind model (ref. 17) for the vertical direction, and an in-line compensator that relates

the feedback control signal to the actuator input signal. When all of these models are combined as in appendix A, the state-space equation of motion for the complete system is

$$\dot{X}_m = A_m X_m + B_m A_c + D_m X_d \quad (1)$$

with X_m defined as

$$X_m = \begin{bmatrix} \dot{X}_w \\ X_w \\ X_a \\ X_f \end{bmatrix} \quad (2)$$

where A_m is the open-loop-model state matrix, B_m is the open-loop-model control input matrix, D_m is the open-loop-model disturbance input matrix, X_m and \dot{X}_m represent the state vector and its time derivative for the open-loop model, A_c is the control feedback signal, X_d is the external-disturbance state vector, X_w and \dot{X}_w represent the wing state vector and its time derivative, X_a is the unsteady aerodynamic state vector, and X_f is the compensator state vector. (A list of symbols used in this paper appears after the references.) A block diagram of the open-loop-system model is shown in figure 2.

MODAL ANALYSIS

Modal analysis is an approach for transforming the system (eq. (1)) into an equivalent number of decoupled state-space equations. The rationale for this approach is that the decoupled equations allow added insight into the control problem. Stability feedback gains can be calculated with only the two complex unstable flutter-mode equations by either a classical control approach or modern control theory. Since the equations are decoupled, theoretical solutions are known and can be used. These ideas are illustrated in this section.

The state vector X_m is transformed to a modal-amplitude vector c_m with the real form of the eigenvector matrix U_m as follows:

$$X_m = U_m c_m \quad (3)$$

Inserting equation (3) into equation (1) yields the modal equation of motion

$$\dot{c}_m = \Lambda_m c_m + G_m A_c + [U_m^{-1} D_m] X_d \quad (4)$$

where

$$\Lambda_m = U_m^{-1} A_m U_m \quad (5)$$

$$G_m = U_m^{-1} B_m \quad (6)$$

and

$$G_m = \begin{bmatrix} g_{m,1} \\ \vdots \\ g_{m,i} \\ \vdots \\ g_{m,n} \end{bmatrix} \quad (14)$$

The solution and form for ϕ_m are shown later.

The solution for Φ_m is

$$\Phi_m = \exp(\Lambda_m T) \quad (15)$$

with block element

$$\phi_{m,i} = \exp(\alpha_i T) \quad (16)$$

for $\lambda_{m,i}$ real and distinct and

$$\phi_{m,i} = \exp(\alpha_i T) \begin{bmatrix} \cos \omega_i T & \sin \omega_i T \\ -\sin \omega_i T & \cos \omega_i T \end{bmatrix} \quad (17)$$

for $\lambda_{m,i}$ complex.

The solution for Γ_m is

$$\Gamma_m = \int_0^T \Phi_m(t - \tau) d\tau \quad (18)$$

The block element is

$$\gamma_{m,i} = \left(\frac{1}{\alpha_i} \right) (\exp(\alpha_i T) - 1) \quad (19)$$

for $\lambda_{m,i}$ real and distinct and is

$$\gamma_{m,i} = \left(\frac{1}{\alpha_i^2 + \omega_i^2} \right) \begin{bmatrix} \gamma_{11m,i} & \gamma_{12m,i} \\ -\gamma_{12m,i} & \gamma_{11m,i} \end{bmatrix} \quad (20)$$

for $\lambda_{m,i}$ complex, where

$$\gamma_{11m,i} = (\exp(\alpha_i T))(\alpha_i \cos \omega_i T + \omega_i \sin \omega_i T) - \alpha_i \quad (21)$$

$$\gamma_{12m,i} = (\exp(\alpha_i T))(\alpha_i \sin \omega_i T - \omega_i \cos \omega_i T) + \omega_i \quad (22)$$

The modal equations are now in explicit decoupled form and can now be used to design stability feedback gains. Putting equations (12), (13), and (14) into equation (11), neglecting the disturbance term since it does not affect stability gain design, and partitioning the equations relating to the unstable flutter mode yields the block equation

$$c_{m,i}(T_m) = \phi_{m,i} c_{m,i}(t_0) + [\gamma_{m,i} g_{m,i}] A_c(t_0) \quad (23)$$

The control-feedback signal A_c is related to the modal amplitude $c_{m,i}$ by the control-feedback gain matrix D_c as

$$A_c(t_0) = D_c c_{m,i}(t_0) \quad (24)$$

where

$$D_c = [k_{1c} \quad k_{2c}] \quad (25)$$

since there is one control surface and two modal amplitudes relating to the complex, unstable flutter mode. In this paper, a pole-placement technique is used; the derivation of the feedback gains for the pole-placement approach is given in appendix B.

The closed-loop equation for the controlled mode is determined by substituting equation (24) into equation (23) as follows:

$$c_{m,i}(T_m) = [\phi_{m,i} + \gamma_{m,i} g_{m,i} D_c] c_{m,i}(t_0) \quad (26)$$

For stability, the eigenvalues of the 2×2 closed-loop matrix must have a magnitude less than unity. It is assumed that all $\phi_{m,i}$, except the term relating to the flutter mode, have open-loop eigenvalues located within the unit circle. This design procedure assumes that higher order modes are influenced as little as possible. Stability of the total closed-loop system is described in a later section.

ESTIMATOR MODEL FOR WIND GUST AND EXTERNAL-DISTURBANCE STATES

If the modal amplitudes $c_{m,i}$ of equation (23) could be measured directly, the stability problem would be solved. Unfortunately, only physical states can be measured, and these states are related to all c_m (eq. (11)). Therefore, an estimator is required to obtain the modal amplitudes in the feedback configuration described previously.

During the period of this research, it became obvious that the wind-gust velocity W_g and the external-disturbance state vector X_d must be estimated to get a good approximation of the two unstable modal-amplitude coordinates. One approach is to augment the states in equation (2) with X_d and W_g and then solve the modal equations as described previously. The approach used in this paper is to augment the modal equation (eq. (11)) after solving for the discrete solutions for W_g and X_d and the effect of W_g and X_d on c_m , given as matrix ϕ_m in that equation.

The wind gust is assumed to have a first-order, slowly varying time response with time constant τ_g defined as

$$\dot{W}_g = -\frac{1}{\tau_g} W_g \quad (27)$$

with the solution

$$W_g(T_m) = \exp(-T/\tau_g) W_g(t_0) \quad (28)$$

The differential equation representing the external disturbance is

$$\dot{X}_d = A_d X_d + B_d W_g \quad (29)$$

where A_d and B_d are the external-disturbance state matrix and forcing-function input matrix. The solution, for a step input W_g applied to a zero-order hold, is

$$X_d(T_m) = \exp(A_d T) X_d(t_0) + A_d^{-1} [\exp(A_d T) - I] B_d W_g(t_0) \quad (30)$$

for A_d nonsingular. The two eigenvalues of A_d are defined as λ_{1d} and λ_{2d} and are used in the solution for ϕ_m . For simplicity, we can define

$$\phi_d = \exp(A_d T) \quad (31)$$

and

$$\Gamma_d = A_d^{-1} [\exp(A_d T) - I] B_d \quad (32)$$

and substitute into equation (30) as follows:

$$X_d(T_m) = \phi_d X_d(t_o) + \Gamma_d W_g(t_o) \quad (33)$$

The general solution for ϕ_m in equation (11) results from solving the forcing-function disturbance term in equation (4) as follows:

$$[\phi_m(X_d, t_o, T_m)] X_d(t_o) = \int_{t_o}^{T_m} [\Phi_m(t - \tau)] [U_m^{-1} D_m] \{X_d(\tau)\} d\tau \quad (34)$$

The solution to this equation requires the use of equations (A21), (A23), (28), and (33) and the solution to three convolution integrals. The derivation is given in appendix C. For the text of this paper, ϕ_m is defined as

$$\phi_m = [\psi_g \quad \psi_d] \quad (35)$$

where ψ_g and ψ_d relate the initial wind-gust velocity and external-disturbance state to the modal-coordinate states. Using these augmented states from equations (28), (33), and (35) and inserting them into equation (11) yields the equation for the discrete modal state vector X_o :

$$X_o(T_m) = A_o X_o(t_o) + B_o A_c(t_o) + L_o \xi(t_o) \quad (36)$$

where

$$X_o = \begin{bmatrix} C_m \\ W_g \\ X_d \end{bmatrix} \quad (37)$$

$$A_o = \begin{bmatrix} \Phi_m & \psi_g & \psi_d \\ 0 & \exp(-T/\tau_g) & 0 \\ 0 & \Gamma_d & \phi_d \end{bmatrix} \quad (38)$$

$$B_o = \begin{bmatrix} \Gamma_m G_m \\ 0 \\ 0 \end{bmatrix} \quad (39)$$

and L_o is a vector relating the external wind ξ to the state vector X_o . For this paper, L_o is defined as the middle-column vector in equation (38). The augmented states W_g and X_d also cause changes in the form of equation (1). By making use of equation (3), the acceleration at time T_m is

$$\dot{X}_m(T_m) = \begin{bmatrix} A_m U_m & W_m & F_m \end{bmatrix} X_o(T_m) + B_m A_c(t_o) \quad (40)$$

where W_m and F_m are part of the derivation given in appendix C.

The measured acceleration output $Y_o(T_m)$, assuming negligible sensor dynamics, is defined as

$$Y_o(T_m) = C_o X_o(T_m) + D_o A_c(t_o) + \theta_o(T_m) \quad (41)$$

where θ_o is measurement noise,

$$C_o = G_o \begin{bmatrix} A_m U_m & W_m & F_m \end{bmatrix} \quad (42)$$

$$D_o = G_o B_m \quad (43)$$

and G_o is a transfer matrix with the number of rows equal to the number of measurements. Each row of G_o has all 0's and a 1 located in the column corresponding to the state that is being measured.

KALMAN-FILTER MODEL

The discretized model of the system dynamics and output measurement is described by equations (36) and (41) and is shown in the upper portion of figure 3. Initial conditions for this model are explained below. The initial state vector $X_o(0)$ is assumed to be a random vector with Gaussian distribution and has an expected value

$$E\{X_o(0)\} = \bar{X}_o(0) = \hat{X}_o(0) \quad (44)$$

where \hat{X}_o is the best estimate of the initial state vector.

The covariance P is defined as

$$\text{cov}[\tilde{X}_o(0); \tilde{X}_o^T(0)] = P(0) > [0] \quad (45)$$

where the variance \tilde{x}_o is

$$\tilde{x}_o = x_o - \bar{x}_o(0) \quad (46)$$

With similar notation for other variables, the Gaussian, discrete white plant noise ξ is

$$E\{\xi(t)\} = 0 \quad (47)$$

and the covariance is

$$\text{cov}[\xi(t); \xi^T(\tau)] = \bar{\xi} \delta_{t\tau} \quad (48)$$

where $\bar{\xi}$ is the plant-noise intensity and $\delta_{t\tau}$ is the Kronecker delta defined as

$$\left. \begin{aligned} \delta_{t\tau} &= 1 & (t = \tau) \\ \delta_{t\tau} &= 0 & (t \neq \tau) \end{aligned} \right\} \quad (49)$$

Similarly, the Gaussian, discrete white measurement noise θ_o is

$$E\{\theta_o(t)\} = 0 \quad (50)$$

and covariance is

$$\text{cov}[\theta_o(t); \theta_o^T(\tau)] = \bar{\theta}_o \delta_{t\tau} \quad (51)$$

where $\bar{\theta}_o$ is the measurement-noise intensity. In addition, $x_o(0)$, $\xi(t)$, and $\theta_o(\tau)$ are mutually independent for all t and τ .

With equations (48) and (51), the state process noise R is defined as

$$R = L_o \bar{\xi} L_o^T \quad (52)$$

and the variance of measurement noise Q_o is defined as

$$Q_o = \bar{\theta}_o \quad (53)$$

Both R and Q_o are assumed to be constant during a run.

With the above definitions and the definition for conditional probability, the equations for the predict cycle are

$$\hat{X}_O(T_m | t_o) = \hat{A}_O \hat{X}_O(t_o | t_o) + \hat{B}_O A_C(t_o) \quad (54)$$

$$P(T_m | t_o) = A_O P(t_o | t_o) A_O^T + R \quad (55)$$

where \hat{X}_O represents the estimated value of X_O and \hat{A}_O and \hat{B}_O represent approximate matrices for A_O and B_O . The approximated matrices have been used both for off-design cases and for cases with less than full-state estimation.

The equations for the update cycle are:

$$G_k = P(T_m | t_o) C_O^T [C_O P(T_m | t_o) C_O^T + Q_O]^{-1} \quad (56)$$

$$\hat{Y}_O(T_m) = \hat{C}_O \hat{X}_O(T_m | t_o) + \hat{D}_O A_C(t_o) \quad (57)$$

$$\hat{X}_O(T_m | T_m) = \hat{X}_O(T_m | t_o) + G_k \{Y_O(T_m) - \hat{Y}_O(T_m)\} \quad (58)$$

$$P(T_m | T_m) = P(T_m | t_o) - G_k C_O P(T_m | t_o) \quad (59)$$

where G_k is the Kalman gain matrix. The structure for the discrete Kalman-filter model is shown in the lower portion of figure 3.

The one remaining link is the relationship between the estimated state vector \hat{X}_O and the control-feedback signal A_C . The equation relating these variables is

$$A_C(t_o) = D_C G_C \hat{X}_O(t_o | t_o) \quad (60)$$

where G_C is a matrix with two rows of elements that are all 0 except for a 1 in each row located in the columns that allow the two modal-amplitude estimates of the unstable mode to be controlled.

Closed-Loop System

A closed-loop stability check is made by looking at the stability of the Kalman loop by itself and by looking at the complete closed-loop control system that includes both the plant and the Kalman model. By using equations (41), (54), (57), and (58), the updated estimated state vector \hat{X}_O becomes

$$\begin{aligned}
\hat{X}_O(T_m|T_m) &= [\hat{A}_O - G_k \hat{C}_O \hat{A}_O] \hat{X}_O(t_o|t_o) \\
&+ [\hat{B}_O - G_k [\hat{C}_O \hat{B}_O + \hat{D}_O - D_O]] A_C(t_o) \\
&+ G_k C_O X_O(T_m) + G_k \theta_O(T_m)
\end{aligned} \tag{61}$$

Stability of the Kalman loop requires that the eigenvalues of $[\hat{A}_O - G_k \hat{C}_O \hat{A}_O]$ lie within the unit circle. The state equations for the complete discrete closed-loop system are

$$\begin{Bmatrix} X_O(T_m) \\ \hat{X}_O(T_m|T_m) \end{Bmatrix} = \begin{bmatrix} S_{11} & S_{12} \\ S_{21} & S_{22} \end{bmatrix} \begin{Bmatrix} X_O(T_o) \\ \hat{X}_O(t_o|t_o) \end{Bmatrix} + \begin{bmatrix} L_O \\ G_k C_O L_O \end{bmatrix} \xi(t_o) + \begin{bmatrix} 0 \\ G_k \end{bmatrix} \theta_O(T_m) \tag{62}$$

where

$$S_{11} = A_O \tag{63}$$

$$S_{12} = B_O D_C G_C \tag{64}$$

$$S_{21} = G_k C_O A_O \tag{65}$$

$$S_{22} = \hat{A}_O - G_k \hat{C}_O \hat{A}_O + \hat{B}_O D_C G_C - G_k [\hat{C}_O \hat{B}_O - C_O B_O + \hat{D}_O - D_O] D_C G_C \tag{66}$$

Stability requires that the eigenvalues of the matrix $\begin{bmatrix} S_{11} & S_{12} \\ S_{21} & S_{22} \end{bmatrix}$ lie within the unit circle.

Suboptimal Filter

The optimal Kalman filter for a plant produces a time-varying gain in which the entire state is estimated and sufficient observations are processed to ensure that all the required states are observable. Moreover, in the presence of random, unknown error sources, process noise must be added to maintain an adequate estimate of the state uncertainty. Since this requires the propagation and correction of the state covariance matrix for each observation, it is not always practical to use an optimal filter in a real-time control system. The usual alternative is to simulate the optimal process off-line until the Kalman gain stabilizes, and then use the steady-state Kalman gains as a constant-gain complementary filter. However, even this approach requires the updating of a large state vector and the processing of a large number of observations. It thus becomes pertinent to seek a smaller state vector and fewer observations which could be used to generate a smaller dimension, constant yet stable gain. Such a system is defined to be suboptimal, and the equations used for the suboptimal system in real time are equations (54), (57), (58), and (60). The off-line calculations for the optimal Kalman gain G_k are made assuming full-state estimation, with \hat{A}_O , \hat{B}_O , \hat{C}_O , and \hat{D}_O equal to A_O , B_O , C_O , and D_O .

The results for two different methods of reducing the number of estimated states are presented in this paper. The first method is to partition the matrix after solving for the optimal gain G_k . In particular, the method involves calculation of the reduced matrices by partitioning both rows and columns of A_o , partitioning only rows of B_o , partitioning only columns of C_o , and leaving D_o unmodified. The second method involves calculation of the reduced G_k directly. This is accomplished by using \hat{A}_o and \hat{C}_o in equations (55), (56), and (59). Results for both methods are described hereinafter. The actual states used are presented in the "Results" section.

RESULTS

This section presents the results for two different sets of closed-loop design eigenvalue (pole) locations for the flutter mode. For each set of pole locations, the statistical accuracy of several state variables resulting from wind-gust disturbances is plotted as a function of dynamic pressure. Plots are presented for the case in which perfect modal feedback is used, for the case in which full-state estimation is used, and for a few cases in which reduced-state estimation is used. In addition, some typical data signals and step responses are presented. Stability of the filter and total closed-loop system has been checked with equations (61) and (62) for every case considered.

The system defined by equation (1) has 33 states: X_w has 11 states defined by 5 bending states, 5 torsional states, and 1 control-surface state; \dot{X}_w has 11 states defined by the derivatives of the X_w states; X_a has 10 states, since the unsteady-aerodynamics terms are modeled by a second-order differential equation for each wing panel; and X_f has 1 state. The unsteady aerodynamics is based on Jones' theory for two-dimensional incompressible flow (ref. 14) and is a good approximation to the lift-deficiency function. State X_f is always included, but the compensator can be effectively nullified by setting the numerator and denominator frequencies approximately equal and large compared with the flutter-mode frequency. Figure 4 contains a plot of the open-loop eigenvalues as a function of dynamic pressure for the 10 flexible-wing modes. The first flexible mode is the flutter mode, with flutter onset occurring at approximately 54.0 kPa. All modes have a structural damping ratio of 0.03. Table I contains the open-loop eigenvalues at the design dynamic pressure q of 82.7 kPa. The eigenvalues are numbered for reference. The equivalent open-loop eigenvalues are also shown for the discrete plane with a sampling period of 0.005 sec, which is the period used for all runs in this paper. For this sampling period, modes 19 and 20 have a frequency greater than one-half the sampling frequency.

Stability is the most important aspect in flutter control, and it must be maintained throughout the flight regime. A second important aspect is the wing response and control-surface activity, resulting from a random wind-gust input disturbance (eqs. (A29) and (A30)). The approach used in this paper, for each of the variables recorded, is to normalize the rms value about a zero mean by the rms value about a zero mean of the wind gust σ_{Wg} . The recorded standard deviations are for the wing-tip bending σ_{h_5} , wing-tip angular rotation σ_{α_5} , control-surface deflection σ_{δ} , control-surface angular velocity $\sigma_{\dot{\delta}}$, and the control-torque input command σ_u .

TABLE I.- OPEN-LOOP EIGENVALUES

[q = 82.7 kPa]

Mode	No.	Continuous-plane eigenvalue		Discrete-plane eigenvalue	
		Real	Imaginary	Real	Imaginary
Flexible wing	1	15.98	47.1	1.0530	0.2527
	2	15.98	-47.1	1.0530	-.2527
	3	-38.41	61.4	.7867	.2493
	4	-38.41	-61.4	.7867	-.2493
	5	-5.42	139.8	.7449	.6264
	6	-5.42	-139.8	.7449	-.6264
	7	-6.31	214.0	.4653	.8499
	8	-6.31	-214.0	.4653	-.8499
	9	-8.68	263.5	.2399	.9270
	10	-8.68	-263.5	.2399	-.9270
	11	-8.93	306.1	.0384	.9556
	12	-8.93	-306.1	.0384	-.9556
	13	-11.19	379.8	-.3050	.8951
	14	-11.19	-379.8	-.3050	-.8951
	15	-13.93	450.1	-.5864	.7253
	16	-13.93	-450.1	-.5864	-.7253
	17	-17.34	605.8	-.9111	.1030
	18	-17.34	-605.8	-.9111	-.1030
	19	-21.10	729.5	-.7872	-.4361
	20	-21.10	-729.5	-.7872	.4361
Actuator/ control surface	21	-357.6	365.1	-0.04216	0.1619
	22	-357.6	-365.1	-.04216	-.1619
Unsteady aerodynamics	23	-72.11		0.6973	
	24	-71.80		.6987	
	25	-70.27		.7037	
	26	-69.18		.7076	
	27	-33.16		.8472	
	28	-10.96		.9467	
	29	-10.93		.9468	
	30	-10.84		.9473	
	31	-10.71		.9479	
	32	-5.78		.9715	
Wind gust	33	-0.6992		0.9966	
External disturbance	34	-31.1		0.8559	
	35	-240.0		.3011	
Compensator	36	-500.0		0.08208	

Two sets of closed-loop pole locations are evaluated. One location is for a low-damped control mode ($\zeta = 0.14$) and the other is for a higher damped control mode ($\zeta = 0.62$); both pole locations have approximately the same damped natural frequency. The two design locations are given in table II for both the continuous and discrete planes. The relationship between the continuous-plane and discrete-plane eigenvalues is given in appendix B.

TABLE II.- DESIGN POLE LOCATIONS FOR CONTROL MODE

Set	Continuous-plane location	Discrete-plane location	Damping ratio
1	$-10 \pm 70j$	$0.89 \pm 0.33j$	0.14
2	$-58 \pm 74j$	$.70 \pm 0.27j$.62

Four different cases have been simulated for each design pole location. The first case, which serves as a reference case for all other data runs, assumes full-state feedback to get a perfect estimate of the unstable modal-amplitude coefficients. In addition, the control-feedback gains D_c are recalculated for each dynamic pressure q in order to maintain the controlled mode at the design pole location. Figures 5 and 6 show the feedback gains used to maintain the controlled mode at the design eigenvalue. For all other runs described in this paper, the feedback gains are kept constant with the values at $q = 82.7$ kPa, shown by the dotted lines in figures 5 and 6.

The other three cases use three output measurements: wing-tip acceleration (grid point 5 in fig. 1), control-surface position, and control-surface angular velocity. All feedback numbers that would be manipulated in a computer (estimator model and stability feedback gains) are maintained constant over the complete range of q .

The second case is for a full-state estimator design (X_o in eq. (37)). For this case, the open- and closed-loop eigenvalue variations of the first two modes are illustrated in figures 7 and 8. These figures are shown in the continuous plane for ease of understanding. For the design eigenvalue at $0.89 \pm 0.33j$, the mode 1 closed-loop eigenvalue shows a small variation, although damping is very small at low values of q . The mode 2 closed-loop eigenvalue illustrates a larger variation than the open-loop case for off-design values of q . With the design eigenvalue of $0.70 \pm 0.27j$, both the mode 1 and mode 2 eigenvalues illustrate a wide variation over the range of q .

The last two cases are for reduced-state estimators (suboptimal filter) and represent different states for the two design pole locations. The partitioning method is used whereby rows and/or columns of nonestimated states are removed from the full-state estimator design. The goal for reduced-state estimation is to reduce the number of computer calculations while maintaining a stable system over the range of q . Table III has the total number of estimated states and the eigenvalue number as given in table I for each design eigenvalue.

TABLE III.- REDUCED-STATE ESTIMATION

Design eigenvalue	Case	Total no. of states	Eigenvalue no.
$0.89 \pm 0.33j$	3	13	1 to 8,21,22,27,33,34
$.89 \pm 0.33j$	4	9	1 to 6,21,22,27
$.70 \pm 0.27j$	3	17	1 to 12,21,22,27,33,34
$.70 \pm 0.27j$	4	15	1 to 12,21,22,27

Notice that fewer flexible-wing modes are required to maintain stability for the low-damped control mode. A possible reason is that the modal amplitude of the lower damped mode is more dominant compared with the higher order modes, making the lower mode more observable in the output measurement compared with the higher damped control mode. Both simulation and analysis have shown that the actuator/control-surface mode must be estimated to maintain stability, while only 1 of the 10 unsteady-aerodynamics modes requires estimation. The mode selected has the largest Kalman gain feedback values of all the unsteady-aerodynamics modes. For stability it is possible to either use or ignore the wind-gust estimate and the external-disturbance states.

Simulation results for the four cases described are illustrated in figures 9 to 18. The first five figures are for the closed-loop design eigenvalue at $0.89 \pm 0.33j$ and the last five figures are for the design eigenvalue at $0.70 \pm 0.27j$. Numbers on each curve correspond to the appropriate case.

Two anomalies are readily observable. The first is that curve 2 shows less bending and less torsional sensitivity to wind-gust disturbance than does curve 1 at high dynamic pressures. One possible explanation is that because the estimator for curve 2 is not optimized for the off-design cases it is probable that the increased modal interaction results in modal contributions that subtract from the overall total. It is just as likely that these contributions add to the total, resulting in a larger state variation. The second anomaly is that at low values of q the control-surface activity is greater for the reference case than for the other three cases. The reason may be that the low-pass filter action in the estimator results in a less sensitive control system than the case with perfect modal feedback.

As expected, cases 3 and 4 show greater activity for rms wind gust than the first two cases. Comparison of the cases shows that less rms variation is obtained by estimating the wind gust and one of the two external-disturbance states. The final data point at $q = 96.5$ kPa is not shown for curve 4 in figures 9 to 13 since both the closed-loop eigenvalues and the simulation data showed an unstable system. In figures 14 to 18 the closed-loop system was barely stable at $q = 96.5$ kPa, and the simulation showed a large increase in the accuracy of each variable.

Several simulation runs were made for cases with measurement noise. A random noise with a standard deviation of 10 percent of the measurement was used for the accelerometer and control-surface angular velocity and a noise with a standard deviation of 1 percent was used for the control-surface position. In addition, a bias error of 0.025g was used for the accelerometer and a bias error of 0.005 rad/sec was used for the control-surface velocity. The simulation runs had statistical data very close to that shown for the perfect-measurement cases.

Some typical simulation plots are shown in figure 19 for the case of full-state estimation. The dynamic pressure was 82.7 kPa and the design eigenvalue was $0.89 \pm 0.33j$ with random and bias measurement errors. The plots in the first part of figure 19 represent the measurements of wing-tip acceleration \ddot{h}_5 , control-surface angular velocity $\dot{\delta}$, and control-surface deflection δ , and wind-gust velocity W_g . The second part of figure 19 contains the wing-tip bending h_5 , wing-tip angular rotation α_5 , wing-tip velocity \dot{h}_5 , and wind-gust velocity W_g . The top two curves in the third part of figure 19 are the actual modal-amplitude coefficients of the controlled mode while the bottom two curves are the estimated modal amplitudes that are used for control.

Figure 20 shows some typical step responses resulting from an external command applied at the same input as feedback signal A_c for $q = 82.7$ kPa with a design eigenvalue of $0.89 \pm 0.33j$. The four cases illustrated are perfect modal estimation (fig. 20(a)), full-state estimation (fig. 20(b)), 13-state estimation (fig. 20(c)), and 9-state estimation (fig. 20(d)). There are seven plots in each figure: h_5 , α_5 , δ , two plots of estimated modal amplitude, and two plots of actual controlled modal amplitude. In figure 20(a), the estimated modal amplitudes are set identical to the controlled modal amplitudes to get the perfect feedback. For full-state estimation, the estimated modal amplitudes are a very good representation of the controlled modal amplitudes, but as the number of estimated states decreases the quality of the estimated modal amplitudes also decreases. The noisy estimates cause increased noise on the control-surface position. The basic responses of the various states are approximately the same for all the cases, although there is a slight attenuation and a little oscillation in the h_5 curve for the reduced-state estimation cases.

A final set of data was taken for another suboptimal-filter case in which the Kalman gain is calculated directly using the reduced matrices \hat{A}_0 and \hat{C}_0 . The results from this approach are generally not as good as the results from the partitioning method. For the reduced-state estimation cases for a design eigenvalue of $0.89 \pm 0.33j$, all data are slightly worse than the data shown in figures 9 to 13. The closed-loop system is unstable at $q = 96.5$ kPa for the 13-state estimation, and the system goes unstable at $q = 89.6$ kPa for the 9-state estimation. For the reduced-state-estimation cases for a design eigenvalue of $0.70 \pm 0.27j$, the data indicate slightly better results for the 15-state-estimation case but worse results for the 17-state-estimation case.

CONCLUSIONS

A modal-control design approach has been used to stabilize a single-control-surface, unswept-wing model subject to bending-torsion flutter. The wing has five panels with five bending and five rotational degrees of freedom in addition to the one control-surface degree of freedom. The complete model also includes unsteady aerodynamics, wind gust, and external-disturbance states relating the wind gust to forces and moments on the wing.

The modal analysis shows the relationship between the physical and the modal domains and the form of the matrices in the modal domain. Since the modal equations of motion are decoupled with block elements of one or two states, analytical solutions can easily be used to obtain feedback gains. The modal approach used in this paper is to partition the two complex-conjugate equations representing the flutter mode and the design feedback gains to stabilize this mode. Only two numbers

are needed to create a stable system. A procedure for calculating these gains for a discrete system for the pole-placement approach used herein is described in appendix B.

The equations for a fixed-gain discrete Kalman filter with a reduced number of output measurements are described. The analysis includes equations for the estimator stability and for the stability of the total closed-loop system. Two approaches for using a suboptimal filter are included.

Statistical data runs using a random wind-gust disturbance have been made for two different closed-loop design-eigenvalue locations for the controlled mode. One eigenvalue location is for a low-damped case (0.14 damping ratio) and the other is for a higher damped case (0.62 damping ratio). With three output measurements (wing-tip acceleration, control-surface position, and control-surface angular velocity), the full-state estimator (36 states) stabilizes the wing over a dynamic-pressure range that is 80 percent greater than that of the uncontrolled system. The design point is at a 50-percent increase in dynamic pressure, and the feedback gains are maintained constant for all off-design dynamic pressures.

Stability can be maintained with fewer estimated states for the low-damped eigenvalue case than for the higher damped case. For the low-damped eigenvalue case, a 13-state estimator model allows stability to be maintained over the entire dynamic-pressure range with only a small decrease in performance, while a 9-state estimator model allows stability to be maintained over most of the range (68-percent increase in dynamic pressure). Simulation runs were made for both the 17-state and the 15-state estimator models for the higher damped eigenvalue case. Both models allow stability to be maintained over the complete dynamic pressure range with a small decrease in performance. The best performance results are obtained in the cases where wind gust and an external-disturbance state are estimated. Random measurement errors with a standard deviation of 10 percent of the measurement for both wing-tip acceleration and control-surface angular velocity and 1-percent standard deviation for control-surface deflection, along with small bias errors, appear to have negligible effect on all of the runs described.

All the data shown for the reduced-state estimators are for the approach where the reduced states are obtained by partitioning rows and/or columns of the matrices in the full-state estimator design. The partitioning method shows better stability and generally less state variations due to wind gust than the approach where the reduced Kalman gains matrix is calculated directly using a reduced plant model.

Langley Research Center
National Aeronautics and Space Administration
Hampton, VA 23665
March 26, 1982

APPENDIX A

MATRICES FOR DEVELOPMENT OF SUBSYSTEM MODELS

This appendix contains the definitions and forms of all matrices used to develop the structural model, the aerodynamics model, the external-disturbance model, the wind-gust model, and the compensator model. In addition, a derivation for the structural-damping model is included. Most of the data for the structural matrices and the steady-state aerodynamics influence coefficients come from reference 13.

Structural Equation of Motion

The state vector X_w for the wing is defined to have 11 states:

$$X_w = \begin{bmatrix} \bar{h}_w \\ \alpha_w \\ \delta \end{bmatrix} \quad (A1)$$

where \bar{h}_w is the 5-state bending displacement with positive axis down, α_w is the 5-state torsional rotation with positive leading edge up, and δ is the trailing-edge control-surface displacement corresponding to trailing edge down. (A list of symbols used in the appendixes appears after the references.) The equation of motion for the wing structure is

$$M_{S_w} \ddot{X}_w + C_{S_w} \dot{X}_w + K_{S_w} X_w = G_s u + L_a + L_d \quad (A2)$$

where M_s , C_s , and K_s represent the structural matrices for the mass-inertia terms, damping terms, and wing bending/torsional-stiffness terms, G_s represents the control-torque input matrix, u represents the control-torque input variable, L_a represents the aerodynamic lift and moments, and L_d represents the external-disturbance forces and moments. The individual matrices are defined below. A deviation of C_s is included at the end of this appendix.

The structural mass-inertia matrix M_s is defined as

$$M_s = \begin{bmatrix} M_w & S_w & S_\delta \\ S_w & J_w & H_\delta \\ \bar{S}_\delta^T & \bar{H}_\delta^T & J_\delta \end{bmatrix} \quad (A3)$$

where

$$S_\delta = \begin{bmatrix} \bar{S}_{\delta 1} V_{\delta 1} \\ \vdots \\ \bar{S}_{\delta 5} V_{\delta 5} \end{bmatrix} \quad (A4)$$

APPENDIX A

$$H_{\delta} = \begin{bmatrix} \bar{H}_{\delta 1} V_{\delta 1} \\ \vdots \\ \bar{H}_{\delta 5} V_{\delta 5} \end{bmatrix} \quad (A5)$$

and M_w is a diagonal mass matrix, J_w is a diagonal inertia matrix, S_w is a diagonal mass-unbalance matrix, \bar{S}_{δ} is a control-surface mass-unbalance vector, \bar{H}_{δ} is a control-surface moment of inertia vector, J_{δ} is the moment of inertia about the control hinge, and V_{δ} defines the wing panel containing the control surface as

$$V_{\delta} = [0 \quad 0 \quad 1 \quad 0 \quad 0]^T \quad (A6)$$

The wing structural-stiffness matrix K_s is defined as

$$K_s = \begin{bmatrix} K_h & 0 & 0 \\ 0 & K_{\alpha} & 0 \\ 0 & 0 & J_{\delta} \omega_{\delta}^2 \end{bmatrix} \quad (A7)$$

where K_h is the bending-stiffness matrix, K_{α} is the torsional-stiffness matrix, and ω_{δ} is the control-surface structural radian frequency. Both K_h and K_{α} are full matrices and are calculated by taking the inverse of their respective flexibility matrices.

The control-torque input matrix G_s is defined as

$$G_s = \begin{bmatrix} 0 \\ -V_{\delta} \\ 1 \end{bmatrix} \quad (A8)$$

The matrix G_s has one column relating to the single control surface being used. In this analysis, the control is modeled as a torque. The actuator torque is applied to the control-surface rotation axis, and an equal and opposite torque is applied directly to the corresponding wing section.

Aerodynamics Model

The unsteady-aerodynamics model contains Jones' exponential approximation of Wagner's indicial loading function for incompressible two-dimensional flow (refs. 14 and 15) as a scalar multiplier of the three-dimensional steady-state lift and moment

APPENDIX A

distribution for the wing. Jones assumed a time-response function $K_a(t)$ as follows:

$$K_a(t) = 1 - 0.165 \exp\left(-0.0455 \frac{Vt}{b}\right) - 0.335 \exp\left(-0.3 \frac{Vt}{b}\right) \quad (A9)$$

where V is the airspeed and b is the semichord. The unsteady-aerodynamics states X_a are functions of both the wing-position states X_w and wing-velocity states \dot{X}_w as follows:

$$\dot{X}_a = A_a X_a + B_{1a} \dot{X}_w + B_{2a} X_w \quad (A10)$$

In return, X_a causes changes in L_a as follows:

$$L_a = C_a X_a + D_{1a} \dot{X}_w + D_{2a} X_w \quad (A11)$$

where X_a is defined to have two five-element states X_{1a} and X_{2a} :

$$X_a = \begin{bmatrix} X_{1a} \\ X_{2a} \end{bmatrix} \quad (A12)$$

since $K_a(t)$ is shown to have a second-order response.

The aerodynamics matrices are defined as the following:

$$D_{1a} = -\left(\frac{g}{2V}\right) \begin{bmatrix} A & AL & k_{\delta}^{ALV} \delta \\ EA & EAL & k_{\delta}^{EALV} \delta \\ \bar{C}^T A & \bar{C}^T AL & k_{\delta}^{\bar{C}^T ALV} \delta \end{bmatrix} \quad (A13)$$

$$D_{2a} = -\left(\frac{g}{2}\right) \begin{bmatrix} 0 & A & k_{\delta}^{AV} \delta \\ 0 & EA & k_{\delta}^{EAV} \delta \\ 0 & \bar{C}^T A & k_{\delta}^{\bar{C}^T AV} \delta \end{bmatrix} \quad (A14)$$

APPENDIX A

$$C_a = (q) \begin{bmatrix} A \\ EA \\ C^T A \end{bmatrix} \left[\left(0.006825 \frac{V}{b^2} \right) I \quad \left(\frac{0.10805}{b} \right) I \right] \quad (A15)$$

$$B_{1a} = \begin{bmatrix} 0 & 0 & 0 \\ \bar{I} & L & k_{\delta} L V_{\delta} \end{bmatrix} \quad (A16)$$

$$B_{2a} = (V) \begin{bmatrix} 0 & 0 & 0 \\ 0 & I & k_{\delta} V_{\delta} \end{bmatrix} \quad (A17)$$

$$A_a = \begin{bmatrix} 0 & I \\ \left(-0.01365 \frac{V^2}{b^2} \right) I & \left(-0.3455 \frac{V}{b} \right) I \end{bmatrix} \quad (A18)$$

where

$$\bar{C}^T = V_{\delta}^T \bar{C}_{\delta} \quad (A19)$$

$$q = \frac{1}{2} \rho V^2 \quad (A20)$$

and where A is the influence-coefficient matrix for the steady-state aerodynamic lift distribution, E is a diagonal matrix with elements equal to the distance between the elastic axis and the aerodynamic center at the i th station, \bar{C}_{δ} is a diagonal matrix with elements equal to the distance from the center of pressure of the control surface to the hinge, L is a diagonal matrix with elements equal to the distance from the three-quarters of the chord to the elastic axis, k_{δ} is the ratio of control-surface lift slope to wing-section lift slope at the wing section containing the control surface, q is the dynamic pressure, ρ is the density, I is an identity matrix, V is the airspeed, and b is the wing semichord.

External-Disturbance Model

The time response K_d for the external disturbance has a form similar to that for the unsteady aerodynamics. The model used is the Küssner function (ref. 16) for the indicial response to a step of vertical gust velocity defined as

$$K_d(t) = 1 - 0.5 \left[\exp\left(-0.13 \frac{vt}{b}\right) + \exp\left(-\frac{vt}{b}\right) \right] \quad (A21)$$

APPENDIX A

In a manner similar to the wing unsteady lift and moment, the two-dimensional response K_d is used as a scalar multiplier to the steady-state three-dimensional aerodynamic lift and moment distribution. As shown in equation (29), the differential equation for the external-disturbance state vector X_d is a function of the wind-gust velocity W_g :

$$\dot{X}_d = A_d X_d + B_d W_g$$

with

$$L_d = C_d X_d \tag{A22}$$

Since K_d is a second-order response, X_d has two states:

$$X_d = \begin{bmatrix} X_{1d} \\ X_{2d} \end{bmatrix} \tag{A23}$$

The matrices for external-disturbance states are the following:

$$C_d = (q) \begin{bmatrix} A \\ EA \\ \bar{C}^T A \end{bmatrix} \begin{Bmatrix} 1 \\ 1 \\ 1 \\ 1 \end{Bmatrix} \left[0.13 \frac{V}{b^2} \quad \frac{0.565}{b} \right] \tag{A24}$$

$$A_d = \begin{bmatrix} 0 & 1 \\ -0.13 \frac{V^2}{b^2} & -1.13 \frac{V}{b} \end{bmatrix} \tag{A25}$$

$$B_d = \begin{bmatrix} 0 \\ 1 \end{bmatrix} \tag{A26}$$

Wind-Gust Model

A Dryden wind model is used to simulate W_g for the transverse direction. The Dryden spectra ϕ_{W_g} for turbulence velocity (ref. 17) is

$$\phi_{W_g}(\Omega_g) = \sigma_g^2 \frac{L_g [1 + 3(L_g \Omega_g)^2]}{\pi [1 + (L_g \Omega_g)^2]^2} \tag{A27}$$

APPENDIX A

where Ω_g is the spatial frequency, L_g is the wind-turbulence scale length (533 m (1750 ft) in ref. 17), and σ_g is the rms wind-gust intensity. By using the relationship between spatial frequency and temporal frequency ω_g as

$$\omega_g = \Omega_g V \quad (A28)$$

and by assuming a discrete random-number generator with sampling period T_g and band-pass frequency $2\pi/T_g$, the equations of motion and matrices become

$$\dot{X}_g = A_g X_g + B_g W_g \quad (A29)$$

and

$$W_g = C_g X_g \quad (A30)$$

where X_g has two states and W_g is the white noise of unit intensity.

The matrices for the wind-gust model are the following:

$$A_g = \begin{bmatrix} 0 & 1 \\ -\gamma_g^2 & -2\gamma_g \end{bmatrix} \quad (A31)$$

$$B_g = \begin{bmatrix} 0 \\ 1 \end{bmatrix} \quad (A32)$$

$$C_g = \left(\sigma_g \sqrt{\frac{6\gamma_g}{T_g}} \right) \begin{bmatrix} -\frac{\gamma_g}{\sqrt{3}} & 1 \end{bmatrix} \quad (A33)$$

where

$$\gamma_g = \frac{V}{L_g} \quad (A34)$$

Compensator Model

There are occasions when in-line compensation, such as a lag circuit, a lead circuit, or a combination, is to be installed. A compensator has been installed at the input to the actuator and is driven by a control-feedback signal A_c as follows:

$$\dot{X}_f = A_f X_f + B_f A_c \quad (A35)$$

and

$$u = C_f X_f + E_f A_c \quad (A36)$$

where A_f , B_f , C_f , and E_f are compensator matrices and X_f is the compensator state. Given a transfer function with a lead frequency ω_{1f} and a lag frequency ω_{2f} , and a gain E_f , the compensator terms become

$$A_f = -\omega_{2f} \quad (A37)$$

$$C_f = \omega_{1f} - \omega_{2f} \quad (A38)$$

$$B_f = E_f = \omega_{2f}/\omega_{1f} \quad (A39)$$

Complete Model

The equations described previously are combined in block diagram form representing the complete open-loop system in figure 21. The key equations are given in the blocks and the equation numbers are given above the blocks. The measured output Y_o is shown as a function of all the states (eq. (41)). Equation (A2) requires some rearranging to get it into proper form for analysis. Combining equations (A11), (A22), and (A36) with equation (A2) yields

$$\ddot{X}_w = D_w \dot{X}_w + A_w X_w + G_a X_a + G_f X_f + G_d X_d + B_c A_c \quad (A40)$$

where

$$\left. \begin{aligned} D_w &= M_s^{-1} [-C_s + D_{1a}] \\ A_w &= M_s^{-1} [-K_s + D_{2a}] \\ G_a &= M_s^{-1} C_a \\ G_d &= M_s^{-1} C_d \\ G_f &= M_s^{-1} G_s C_f \\ B_c &= M_s^{-1} G_s E_f \end{aligned} \right\} \quad (A41)$$

APPENDIX A

With these definitions, the matrices for equation (1) are

$$A_m = \begin{bmatrix} D_w & A_w & G_a & G_f \\ I & 0 & 0 & 0 \\ B_{1a} & B_{2a} & A_a & 0 \\ 0 & 0 & 0 & A_f \end{bmatrix} \quad (A42)$$

$$B_m = \begin{bmatrix} B_c \\ 0 \\ 0 \\ B_f \end{bmatrix} \quad (A43)$$

$$D_m = \begin{bmatrix} G_d \\ 0 \\ 0 \\ 0 \end{bmatrix} \quad (A44)$$

Derivation for Structural-Damping Matrix C_s

The homogeneous differential equation for the wing structure is

$$M_s \ddot{X}_w + C_s \dot{X}_w + K_s X_w = 0 \quad (A45)$$

By using the modal transformation,

$$X_w = U_s Z_s \quad (A46)$$

The equation of motion in modal form becomes

$$\ddot{Z}_s + D_s \dot{Z}_s + \Lambda_s Z_s = 0 \quad (A47)$$

where

$$D_s = U_s^{-1} M_s^{-1} C_s U_s \quad (A48)$$

APPENDIX A

$$\Lambda_s = U_s^{-1} M_s^{-1} K_s U_s \quad (A49)$$

Equation (A47) is completely decoupled with each differential state equation of the form

$$\ddot{z}_{s,i} + 2\zeta_{s,i}\omega_{s,i}\dot{z}_{s,i} + \omega_{s,i}^2 z_{s,i} = 0 \quad (A50)$$

where $\omega_{s,i}$ is the radian frequency for mode i and $\zeta_{s,i}$ is the structural damping ratio for mode i . The matrix Λ_s is calculated by letting the damping ratio be 0 in equation (A45) and solving for the eigenvalues. The matrix D_s is determined next by inputting approximate values for ζ_s . With equation (A48), C_s is calculated as

$$C_s = M_s U_s D_s U_s^{-1} \quad (A51)$$

APPENDIX B

DERIVATION OF FEEDBACK GAINS FOR POLE-PLACEMENT APPROACH

This appendix presents the derivation and final equations for calculating the stability feedback gains for a discrete control system, in which the desired pole locations are either in the unit circle for discrete pole placement or in the standard S-plane for continuous pole placement. The derivation is for a complex-conjugate plant with one control input A_c .

The modal equation of motion is given in equation (4):

$$\dot{c}_m(t) = \Lambda_m c_m(t) + G_m A_c(t_0)$$

and the discrete form solution for the unstable flutter mode is presented in equation (23):

$$c_m(T_m) = \phi_m c_m(t_0) + [\gamma_m g_m] A_c(t_0)$$

Equations (24) and (25) define the control feedback as

$$A_c(t_0) = D_c c_m(t_0)$$

where

$$D_c = [k_{1c} \quad k_{2c}]$$

Finally, the closed-loop expression in equation (26) is

$$c_m(T_m) = [\phi_m + \gamma_m g_m D_c] c_m(t_0)$$

In the preceding equations, subscript i is deleted for convenience.

Subscripts m and c and the arguments T_m and t_0 will be dropped in the remainder of this paper for simplicity. If the desired poles λ_d are located in the continuous plane, the first step is to calculate the equivalent poles Z in the discrete plane. Defining λ_d and Z in terms of the real and imaginary parts gives

$$Z_R = \exp(\alpha_d T) \cos(\omega_d T) \tag{B1}$$

$$Z_I = \exp(\alpha_d T) \sin(\omega_d T) \tag{B2}$$

APPENDIX B

where α_d and ω_d are the real and imaginary parts of λ_d , Z_R and Z_I are the real and imaginary parts of Z , and T is the sampling period.

By defining ϕ , γ , and g in terms of their components, equation (23) becomes

$$\begin{Bmatrix} c_1 \\ c_2 \end{Bmatrix} = \begin{bmatrix} \phi_{11} & \phi_{12} \\ -\phi_{12} & \phi_{11} \end{bmatrix} \begin{Bmatrix} c_1 \\ c_2 \end{Bmatrix} + \begin{bmatrix} \gamma_{11} & \gamma_{12} \\ -\gamma_{12} & \gamma_{11} \end{bmatrix} \begin{bmatrix} g_1 \\ g_2 \end{bmatrix} A_c \quad (B3)$$

With the definitions

$$v_1 = \gamma_{11}g_1 + \gamma_{12}g_2 \quad (B4)$$

and

$$v_2 = -\gamma_{12}g_1 + \gamma_{11}g_2 \quad (B5)$$

the closed-loop expression in equation (26) is

$$\begin{Bmatrix} c_1 \\ c_2 \end{Bmatrix} = \begin{bmatrix} \bar{\phi}_{11} & \bar{\phi}_{12} \\ \bar{\phi}_{21} & \bar{\phi}_{22} \end{bmatrix} \begin{Bmatrix} c_1 \\ c_2 \end{Bmatrix} \quad (B6)$$

where

$$\bar{\phi}_{11} = \phi_{11} + v_1 k_{1c} \quad (B7)$$

$$\bar{\phi}_{12} = \phi_{12} + v_1 k_{2c} \quad (B8)$$

$$\bar{\phi}_{21} = -\phi_{12} + v_2 k_{1c} \quad (B9)$$

$$\bar{\phi}_{22} = \phi_{11} + v_2 k_{2c} \quad (B10)$$

The closed-loop eigenvalues of equation (B6) are found by using

$$\begin{vmatrix} z - \bar{\phi}_{11} & -\bar{\phi}_{12} \\ -\bar{\phi}_{21} & z - \bar{\phi}_{22} \end{vmatrix} = 0 \quad (\text{B11})$$

with the solution

$$z = \frac{\bar{\phi}_{11} + \bar{\phi}_{22}}{2} \pm \frac{1}{2} \sqrt{(\bar{\phi}_{11} - \bar{\phi}_{22})^2 + 4\bar{\phi}_{12}\bar{\phi}_{21}} \quad (\text{B12})$$

Substituting equation (B7) into equation (B10) yields

$$z = \frac{2\phi_{11} + v_1 k_{1c} + v_2 k_{2c}}{2} \pm \frac{1}{2} \sqrt{(v_1 k_{1c} + v_2 k_{2c})^2 - 4\phi_{12}(\phi_{12} + v_1 k_{1c} - v_2 k_{2c})} \quad (\text{B13})$$

For complex-conjugate eigenvalues,

$$z = z_R \pm z_I j \quad (\text{B14})$$

Equating the real parts of equations (B13) and (B14) yields

$$k_{2c} = \frac{1}{v_2} (2z_R - 2\phi_{11} - v_1 k_{1c}) \quad (\text{B15})$$

For complex-conjugate eigenvalues, the expression under the radical in equation (B13) is negative. Equating the imaginary parts of equations (B13) and (B14) and substituting equation (B15) yields

$$k_{1c} = \frac{-[z_R^2 + z_I^2] - \phi_{11}^2 + \phi_{12}^2 + 2\phi_{11}z_R + 2\phi_{12}\left(\frac{v_1}{v_2}\right)(z_R - \phi_{11})}{\phi_{12} \frac{(v_1)^2}{v_2} + \phi_{12}v_2} \quad (\text{B16})$$

For the two real eigenvalues, either distinct or equal, z is expressed as

$$z_{R1} = \frac{\bar{\phi}_{11} + \bar{\phi}_{22}}{2} - \frac{1}{2} \sqrt{(\bar{\phi}_{11} - \bar{\phi}_{22})^2 + 4\bar{\phi}_{12}\bar{\phi}_{21}} \quad (\text{B17})$$

APPENDIX B

or

$$z_{R2} = \frac{\bar{\phi}_{11} + \bar{\phi}_{22}}{2} + \frac{1}{2} \sqrt{(\bar{\phi}_{11} - \bar{\phi}_{22})^2 + 4\phi_{12}\phi_{21}} \quad (\text{B18})$$

Adding equations (B17) and (B18) and using equation (B13) yields

$$k_{2c} = \frac{1}{v_2} (z_{R1} + z_{R2} - 2\phi_{11} - v_1 k_{1c}) \quad (\text{B19})$$

Subtracting equation (B19) from equation (B18) and substituting for k_{2c} yields

$$k_{1c} = \frac{-z_{R1}z_{R2} - \phi_{11}^2 + \phi_{12}^2 + \phi_{11}(z_{R1} + z_{R2}) + \phi_{12}\left(\frac{v_1}{v_2}\right)(z_{R1} + z_{R2} - 2\phi_{11})}{\phi_{12}\frac{(v_1)^2}{v_2} + \phi_{12}v_2} \quad (\text{B20})$$

APPENDIX C

DERIVATION FOR TRANSFORMATION MATRIX RELATING EXTERNAL-DISTURBANCE

STATES TO MODAL COORDINATES

The Küssner function is given in equation (A21) of appendix A and the model given in equations (29) and (A23). The solution to the differential equation is shown in equations (30) to (33). The differential equation (eq. (29))

$$\dot{\mathbf{X}}_d = \mathbf{A}_d \mathbf{X}_d + \mathbf{B}_d \mathbf{W}_g$$

and the general solution (eq. (33))

$$\mathbf{X}_d(t_m) = \phi_d \mathbf{X}_d(t_o) + \Gamma_d \mathbf{W}_g(t_o)$$

are repeated here with the following definitions:

$$\phi_d = \begin{bmatrix} \phi_{11d} & \phi_{12d} \\ \phi_{21d} & \phi_{22d} \end{bmatrix} \quad (C1)$$

$$\Gamma_d = \begin{bmatrix} \gamma_{1d} \\ \gamma_{2d} \end{bmatrix} \quad (C2)$$

From equation (A24) and with the following definitions,

$$\mathbf{E}_d = \begin{bmatrix} \mathbf{A} \\ \mathbf{EA} \\ \mathbf{C}^T \mathbf{A} \end{bmatrix} \begin{Bmatrix} 1 \\ 1 \\ 1 \\ 1 \\ 1 \end{Bmatrix} \quad (C3)$$

$$k_{1d} = -0.13 \left(\frac{v^2}{b^2} \right) \quad (C4)$$

$$k_{2d} = -1.13 \frac{v}{b} \quad (C5)$$

the external-disturbance force and moment vector is written as

$$L_d(T_m) = \left(\frac{g}{V}\right) \{E_d\} \left[-k_{1d} X_{1d}(T_m) - \left(\frac{k_{2d}}{2}\right) X_{2d}(T_m) \right] \quad (C6)$$

Substituting equation (33) and combining terms gives

$$L_d(T_m) = \left(\frac{g}{V}\right) \{E_d\} (\phi_{1d} X_{1d}(t_o) + \phi_{2d} X_{2d}(t_o) + \gamma_d W_g(t_o)) \quad (C7)$$

where

$$\phi_{1d} = -k_{1d} \phi_{11d} - 0.5k_{2d} \phi_{21d} \quad (C8)$$

$$\phi_{2d} = -k_{1d} \phi_{12d} - 0.5k_{2d} \phi_{22d} \quad (C9)$$

$$\gamma_d = -k_{1d} \gamma_{1d} - 0.5k_{2d} \gamma_{2d} \quad (C10)$$

With actual values the following are obtained:

$$\phi_{1d} = 0.065 \frac{V}{b} (\exp(\lambda_{1d} T) + \exp(\lambda_{2d} T)) \quad (C11)$$

$$\phi_{2d} = (0.065 \exp(\lambda_{1d} T) + 0.5 \exp(\lambda_{2d} T)) \quad (C12)$$

$$\gamma_d = 1 - 0.5(\exp(\lambda_{1d} T) + \exp(\lambda_{2d} T)) \quad (C13)$$

The general solution for ϕ_m is given in equation (34) as

$$\phi_m(x_d, t_o, T_m) x_d(t_o) = \int_{t_o}^{T_m} [\phi_m(t - \tau)] [U_m^{-1} D_m] \{x_d(\tau)\} d\tau$$

Using equations (A44), (A22), and the solution for G_d in equation (A41) we get

$$\phi_m(x_d, t_o, T_m) x_d(t_o) = \int_{t_o}^{T_m} [\phi_m(t - \tau)] [U_m^{-1}] \begin{bmatrix} M^{-1} \\ -S \\ 0 \end{bmatrix} \{L_d(\tau)\} d\tau \quad (C14)$$

Substituting equation (C7) yields

$$\begin{aligned} \psi_m(X_d, t_o, T_m) X_d(t_o) = & \int_{t_o}^{T_m} [\phi_m(t - \tau)] \{h_m\} (\phi_{1d}(\tau) X_{1d}(t_o) \\ & + \phi_{2d}(\tau) X_{2d}(t_o) + \gamma_d(\tau) W_g(t_o)) d\tau \end{aligned} \quad (C15)$$

where

$$\{h_m\} = \begin{pmatrix} g \\ v \end{pmatrix} [U_m^{-1}] \begin{pmatrix} M^{-1} E_d \\ -s \quad 0 \end{pmatrix} \quad (C16)$$

Rewriting equation (C15) gives

$$\psi_m(X_d, t_o, T_m) X_d(t_o) = \psi_g W_g(t_o) + \psi_{1d} X_{1d}(t_o) + \psi_{2d} X_{2d}(t_o) \quad (C17)$$

where the three convolution integrals are

$$\psi_g = \left[\int_{t_o}^{T_m} [\Phi_m(\tau)] (\gamma_d(t - \tau)) d\tau \right] \{h_m\} \quad (C18)$$

$$\psi_{1d} = \left[\int_{t_o}^{T_m} [\Phi_m(\tau)] (\phi_{1d}(t - \tau)) d\tau \right] \{h_m\} \quad (C19)$$

$$\psi_{2d} = \left[\int_{t_o}^{T_m} [\Phi_m(\tau)] (\phi_{2d}(t - \tau)) d\tau \right] \{h_m\} \quad (C20)$$

By letting

$$\psi_d = [\psi_{1d} \quad \psi_{2d}] \quad (C21)$$

and with equation (35)

$$\psi_m = [\psi_g \quad \psi_d]$$

the discrete solution for the modal coefficients in equation (11) becomes

$$c_m(T_m) = \Phi_m c_m(t_o) + \Gamma_{m m} G A(t_o) + \psi_g W_g(t_o) + \psi_d X_d(t_o) \quad (C22)$$

APPENDIX C

The solution for each convolution integral ϕ_g , ϕ_{1d} , and ϕ_{2d} is shown below. A typical block matrix for Φ_m is given in equations (16) and (17) with elements defined in equations (B1) and (B3). The equations for ϕ_{1d} , ϕ_{2d} , and γ_d are defined in equations (C11) to (C13). Combining all of these equations, the solution for equations (C18), (C19), and (C20) can be determined. The result below does not include the final multiplication by vector h_m , which would only affect the final gains. Since this is a typical block, subscript i is dropped for convenience.

With the definitions

$$e_1 = \exp(\lambda_{1d}T) \quad (C23)$$

$$e_2 = \exp(\lambda_{2d}T) \quad (C24)$$

the elements of each matrix are the following, with equations (C25) and (C26) relating to ϕ_{1d} , equations (C27) and (C28) relating to ϕ_{2d} , and equations (C29) and (C30) relating to ϕ_g :

$$\begin{aligned} \psi_{11,1d} = \psi_{22,1d} = 0.065 \frac{v^2}{b^2} & \left\{ \frac{\omega\phi_{12} + (\alpha - \lambda_{1d})(\phi_{11} - e_1)}{(\alpha - \lambda_{1d})^2 + \omega^2} \right. \\ & \left. + \frac{\omega\phi_{12} + (\alpha - \lambda_{2d})(\phi_{11} - e_2)}{(\alpha - \lambda_{2d})^2 + \omega^2} \right\} \end{aligned} \quad (C25)$$

$$\begin{aligned} \psi_{12,1d} = -\psi_{21,1d} = 0.065 \frac{v^2}{b^2} & \left\{ \frac{\phi_{12}(\alpha - \lambda_{1d}) - \omega(\phi_{11} - e_1)}{(\alpha - \lambda_{1d})^2 + \omega^2} \right. \\ & \left. + \frac{\phi_{12}(\alpha - \lambda_{2d}) - \omega(\phi_{11} - e_2)}{(\alpha - \lambda_{2d})^2 + \omega^2} \right\} \end{aligned} \quad (C26)$$

$$\begin{aligned} \psi_{11,2d} = \psi_{22,2d} = \frac{v}{b} & \left\{ \frac{0.065[\omega\phi_{12} + (\alpha - \lambda_{1d})(\phi_{11} - e_1)]}{(\alpha - \lambda_{1d})^2 + \omega^2} \right. \\ & \left. + \frac{0.5[\omega\phi_{12} + (\alpha - \lambda_{2d})(\phi_{11} - e_2)]}{(\alpha - \lambda_{2d})^2 + \omega^2} \right\} \end{aligned} \quad (C27)$$

$$\begin{aligned} \psi_{12,2d} = -\psi_{21,2d} = \frac{v}{b} & \left\{ \frac{0.065[\phi_{12}(\alpha - \lambda_{1d}) - \omega(\phi_{11} - e_1)]}{(\alpha - \lambda_{1d})^2 + \omega^2} \right. \\ & \left. + \frac{0.5[\phi_{12}(\alpha - \lambda_{2d}) - \omega(\phi_{11} - e_2)]}{(\alpha - \lambda_{2d})^2 + \omega^2} \right\} \end{aligned} \quad (C28)$$

APPENDIX C

$$\phi_{11,g} = \phi_{22,g} = \gamma_{11} - 0.5 \left\{ \frac{\omega\phi_{12} + (\alpha - \lambda_{1d})(\phi_{11} - e_1)}{(\alpha - \lambda_{1d})^2 + \omega^2} + \frac{\omega\phi_{12} + (\alpha - \lambda_{2d})(\phi_{11} - e_2)}{(\alpha - \lambda_{2d})^2 + \omega^2} \right\} \quad (C29)$$

$$\phi_{12,g} = -\phi_{21,g} = \gamma_{12} - 0.5 \left\{ \frac{\phi_{12}(\alpha - \lambda_{1d}) - \omega(\phi_{11} - e_1)}{(\alpha - \lambda_{2d})^2 + \omega^2} + \frac{\phi_{12}(\alpha - \lambda_{2d}) - \omega(\phi_{11} - e_2)}{(\alpha - \lambda_{2d})^2 + \omega^2} \right\} \quad (C30)$$

where γ_{11} and γ_{12} are defined in equations (21) and (22).

Portions of the derivation presented here are also used to derive W_m and F_m , used in equation (40). Equation (1) is given as

$$\dot{X}_m = A_m X_m + B_m A_c + D_m X_d$$

Using equations (A23), (A44), and the solution for G_d in equation (A41) the disturbance term becomes

$$D_m X_d = \left(\frac{q}{v}\right) \begin{bmatrix} M^{-1} C_d \\ -s \quad 0 \end{bmatrix} X_d \quad (C31)$$

Substituting equation (C3) and using the definitions in equations (C8) to (C10) results in

$$D_m X_d = \left(\frac{q}{v}\right) \begin{bmatrix} M^{-1} E_d \\ -s \quad 0 \end{bmatrix} (\gamma_d W_g + \phi_{1d} X_{1d} + \phi_{2d} X_{2d}) \quad (C32)$$

We can now define

$$W_m = \left(\frac{q}{v}\right) \begin{bmatrix} M^{-1} E_d \\ -s \quad 0 \end{bmatrix} (\gamma_d) \quad (C33)$$

$$F_m = \left(\frac{q}{v}\right) \begin{bmatrix} M^{-1} E_d \\ -s \quad 0 \end{bmatrix} [\phi_{1d} \quad \phi_{2d}] \quad (C34)$$

REFERENCES

1. Creedon, J. F.; and Lindgren, A. G.: Control of the Optical Surface of a Thin, Deformable Primary Mirror With Application to an Orbiting Astronomical Observatory. *Automatica*, vol. 6, no. 5, Sept. 1970, pp. 643-660.
2. Howell, W. E.; and Creedon, J. F.: A Technique for Designing Active Control Systems for Astronomical-Telescope Mirrors. NASA TN D-7090, 1973.
3. Ostroff, Aaron J.: Evaluation of Control Laws and Actuator Locations for Control Systems Applicable to Deformable Astronomical Telescope Mirrors. NASA TN D-7276, 1973.
4. Balas, Mark J.: Modal Control of Certain Flexible Dynamic Systems. *SIAM J. Control & Optim.*, vol. 16, no. 3, May 1978, pp. 450-462.
5. Meirovitch, L.; Van Landingham, H. F.; and Öz, H.: Control of Spinning Flexible Spacecraft by Modal Synthesis. *Acta Astronaut.*, vol. 4, no. 9/10, Sept./Oct. 1977, pp. 985-1010.
6. Meirovitch, L.; and Öz, H.: Observer Modal Control of Dual-Spin Flexible Spacecraft. *J. Guid. & Control*, vol. 2, no. 2, Mar.-Apr. 1979, pp. 101-110.
7. Meirovitch, L.; and Öz, H.: Modal-Space Control of Large Flexible Spacecraft Possessing Ignorable Coordinates. *Dynamics and Control of Large Flexible Spacecraft*, L. Meirovitch, ed., American Inst. Aeronaut. & Astronaut., 1979, pp. 701-728.
8. Nissim, E.: Flutter Suppression Using Active Controls Based on a Concept of Aerodynamic Energy. NASA TN D-6199, 1971.
9. Nissim, E.; and Abel, I.: Development and Application of an Optimization Procedure for Flutter Suppression Using the Aerodynamic Energy Concept. NASA TP-1137, 1978.
10. Newsom, Jerry R.: Control Law Synthesis for Active Flutter Suppression Using Optimal Control Theory. *J. Guid. & Control*, vol. 2, no. 5, Sept.-Oct. 1979, pp. 388-394.
11. Gangsaas, D.; Ly, U.; and Norman, D. C.: Practical Gust Load Alleviation and Flutter Suppression Control Laws Based on a LQG Methodology. AIAA-81-0021, Jan. 1981.
12. Gangsaas, Dagfinn; and Ly, Uy-Loi: Application of a Modified Linear Quadratic Gaussian Design to Active Control of a Transport Airplane. AIAA Paper 79-1746, Aug. 1979.
13. Pines, Samuel: A Unit Solution for the Load Distribution of a Nonrigid Wing by Matrix Methods. *J. Aeronaut. Sci.*, vol. 16, no. 8, Aug. 1949, pp. 470-476.
14. Jones, Robert T.: The Unsteady Lift of a Wing of Finite Aspect Ratio. NACA Rep. 681, 1940.

15. Edwards, John William: Unsteady Aerodynamic Modeling and Active Aeroelastic Control. SUDAAR 504 (NASA Grant NGL-05-020-007), Stanford Univ., Feb. 1977. (Available as NASA CR-148019.)
16. Bisplinghoff, Raymond L.; and Ashley, Holt: Principles of Aeroelasticity. John Wiley & Sons, Inc., c.1962.
17. Flying Qualities of Piloted Airplanes. Mil. Specif. MIL-F-8785C, Nov. 5, 1980.

SYMBOLS

Symbols Applicable to Entire Paper

A_c	control-feedback signal
A_d	external-disturbance state matrix
A_m	open-loop-model state matrix
B_d	external-disturbance forcing-function input matrix
B_m	open-loop-model control input matrix
B_o	augmented discrete modal-control input matrix
C_o	augmented discrete output modal state matrix
c_m	modal-amplitude vector
D_c	control-feedback gain matrix
D_m	open-loop-model disturbance input matrix
D_o	augmented discrete output-control input matrix
F_m	discrete matrix relating external disturbances to Y_o
G_c	transformation matrix relating estimated modal-amplitude vector to modal amplitude used for control
G_k	Kalman gain matrix
G_m	control input matrix for modal equation
G_o	transfer matrix for output measurements
$g_{m,i}$	ith element of matrix G_m
$h_{w,i}$	wing displacement for ith panel
h_5	wing displacement for fifth panel
I	identity matrix
j	imaginary number
k_{1c}, k_{2c}	control-feedback gains
L_o	vector relating external random wind to state vector X_o
P	covariance matrix
Q_o	variance of measurement noise

q dynamic pressure
 R state process noise
 $S_{11}, S_{12}, S_{21}, S_{22}$ submatrices for discrete closed-loop state matrix
 s Laplace transform
 T sampling period for control
 T_m time at end of sampling period
 t time
 t_0 initial time
 U_m eigenvector matrix
 u control-torque input
 W_g wind-gust velocity
 W_m discrete matrix relating wind gust to Y_0
 X_a unsteady-aerodynamics state vector
 X_d external-disturbance state vector
 X_f compensator state vector
 X_m state vector for complete open-loop model
 X_0 augmented discrete modal state vector
 X_w wing state vector
 Y_0 measured acceleration-output vector
 α_i real part of eigenvalue $\lambda_{m,i}$
 $\alpha_{w,i}$ wing torsional rotation for i th panel
 α_5 wing torsional rotation for fifth panel
 Γ_d vector defining discrete transformation between initial value of wind gust and external-disturbance state
 Γ_m control input matrix in the discrete modal solution
 $\gamma_{m,i}$ i th element of Γ_m
 δ trailing-edge control-surface displacement
 $\delta_{t\tau}$ Kronecker delta

ζ	damping ratio
θ_o	Gaussian, discrete white measurement noise
$\overline{\theta_o}$	measurement-noise intensity
Λ_m	open-loop eigenvalue matrix
$\lambda_{m,i}$	i th element of Λ_m
$\lambda_{1d}, \lambda_{2d}$	eigenvalues of A_d
ξ	Gaussian, discrete white plant noise
$\overline{\xi}$	process-noise intensity
σ	standard deviation
τ	time variable
τ_g	first-order time constant for wind-gust approximation
Φ_m	discrete modal state transition matrix
ϕ_d	discrete transition matrix for external disturbance
$\phi_{m,i}$	i th element of Φ_m
ψ_d	submatrix of ψ_m
ψ_g	submatrix of ψ_m
ψ_m	discrete transition matrix relating external-disturbance states to the modal-amplitude vector
ω_i	imaginary part of eigenvalue λ_m

Superscripts:

—	mean value
^	estimated value
~	variance
-1	inverse
T	transpose

Special operators:

$E\{ \}$	expected value of a vector
exp	exponential

[] matrix
 cov[] covariance
 (X|Y) conditional density of X given the value of Y

Symbols Applicable to Appendixes Only

A influence-coefficient matrix for the steady-state aerodynamic lift distribution
 A_a unsteady-aerodynamics state matrix
 A_f compensator state matrix
 A_g wind-gust state matrix
 A_w submatrix of A_m
 B_c submatrix of B_m
 B_f compensator-control input matrix
 B_g wind-gust forcing-function input matrix
 B_{1a}, B_{2a} unsteady-aerodynamics forcing-function input matrices
 b wing semichord
 C_a unsteady-aerodynamics output state matrix
 C_d external-disturbance output matrix
 C_f compensator-output state matrix
 C_g wind-gust output matrix
 C_s structural-damping matrix
 \bar{C} defined in equation (A14)
 \bar{C}_0 diagonal matrix with elements equal to the distance from the center of pressure of the control surface to the hinge
 D_s modal structural-damping matrix
 D_w submatrix of A_m
 D_{1a}, D_{2a} unsteady-aerodynamics forcing-function output matrices
 E diagonal matrix with elements equal to the distance between elastic axis and aerodynamic center at the ith station
 E_d defined by equation (C3)

E_f compensator-output-control input matrix
 G_a submatrix of A_m
 G_d submatrix of D_m
 G_f submatrix of A_m
 G_s control-torque input matrix
 H_δ defined by equation (A5)
 \bar{H}_δ control-surface moment of inertia vector
 h_m defined by equation (C16)
 J_w diagonal inertia matrix
 J_δ moment of inertia about the control hinge
 K_a time response for Jones' approximation
 K_d time response for Kussner' function
 K_h bending-stiffness matrix
 K_s wing structural-stiffness matrix
 K_α torsional-stiffness matrix
 k_δ ratio of control-surface lift slope to wing-section lift slope at the wing section containing the control surface
 k_{1d}, k_{2d} constants
 L diagonal matrix with elements equal to the distance from three-quarters of the chord to the elastic axis
 L_a aerodynamic lift and moment vector
 L_d external-disturbance force and moment vector
 L_g wind-turbulence scale length
 M_s matrix containing structural mass and inertia terms
 M_w diagonal mass matrix
 S_w diagonal mass-unbalance matrix
 S_δ defined by equation (A4)
 \bar{S}_δ control-surface mass-unbalance vector
 T_g sampling period for wind-gust random-number generator

U_s modal transformation for free vibration
 V airspeed
 V_δ wing panel containing control surface
 v_1, v_2 defined respectively in equations (B4) and (B5)
 W_c white noise of unit intensity
 X_g wind-gust state vector
 X_{1a}, X_{2a} components of unsteady-aerodynamics state vector X_a
 X_{1d}, X_{2d} components of external-disturbance state vector X_d
 Z_I discrete-plane imaginary root
 Z_R discrete-plane real root
 Z_s structural modal coordinate
 α_d real part of desired pole
 γ_d defined in equation (C10)
 γ_g band-pass frequency for wind model
 γ_{1d}, γ_{2d} components of Γ_d
 γ_{11}, γ_{12} elements of matrix $\gamma_{m^g m}$
 Λ_s diagonal eigenvalue matrix for structure
 λ_d desired pole
 σ_g wind-gust intensity
 ϕ_{11}, ϕ_{12} elements of the open-loop discrete modal transition matrix
 $\phi_{11d}, \phi_{12d}, \phi_{21d}, \phi_{22d}$ components of ϕ_d
 $\bar{\phi}_{11}, \bar{\phi}_{12}, \bar{\phi}_{21}, \bar{\phi}_{22}$ elements of the closed-loop discrete modal transition matrix
 ϕ_{Wg} Dryden spectra
 Ω_g spatial frequency for wind-gust model
 ω_d imaginary part of desired pole
 ω_g temporal frequency for wind-gust model

ω_{1f}, ω_{2f} compensator frequencies

ω_{δ} control-surface structural radian frequency

One dot over a symbol indicates first derivative with respect to time. Two dots over a symbol indicate second derivative with respect to time.

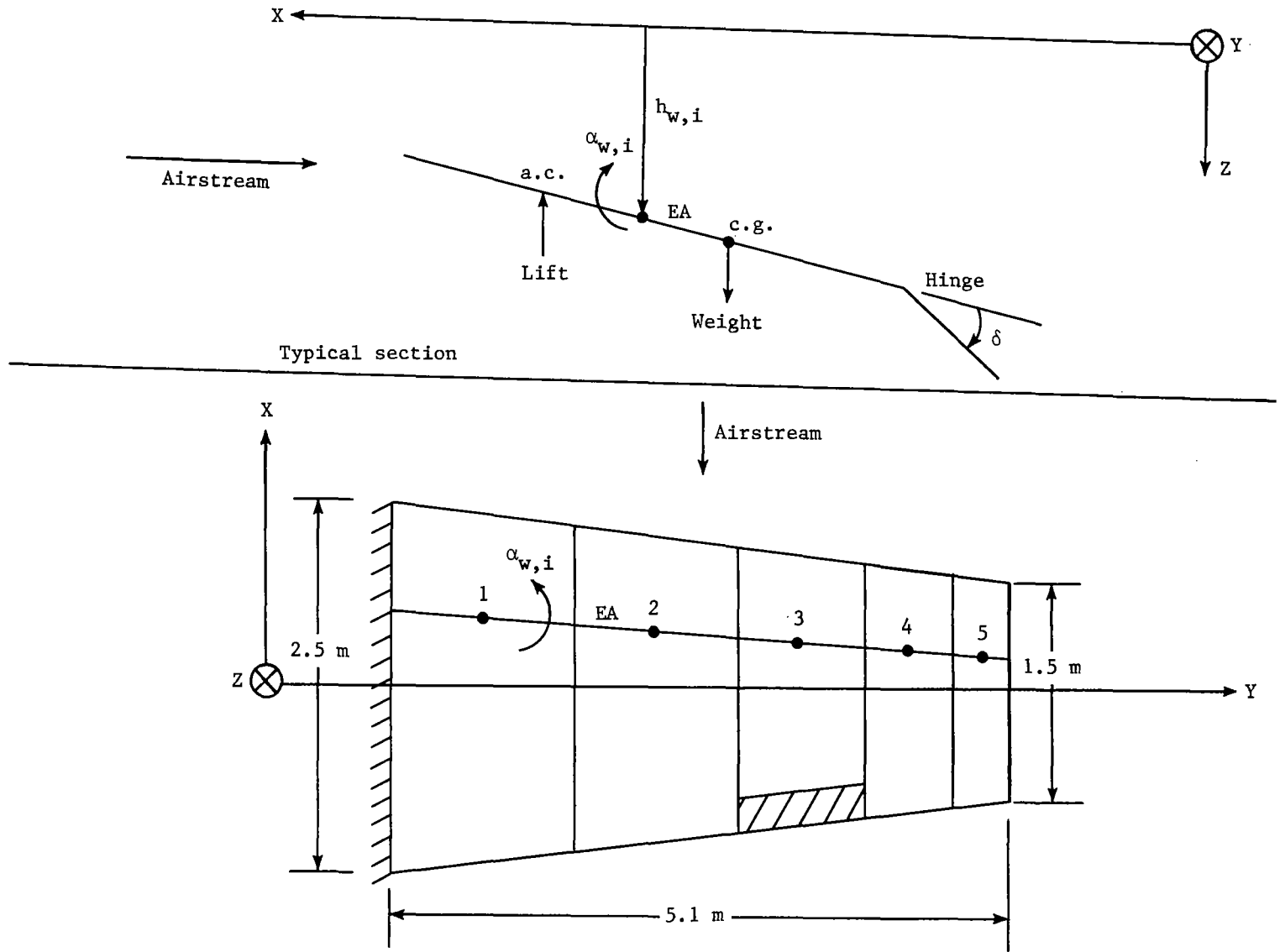


Figure 1.- Simplified model of unswept aircraft wing.

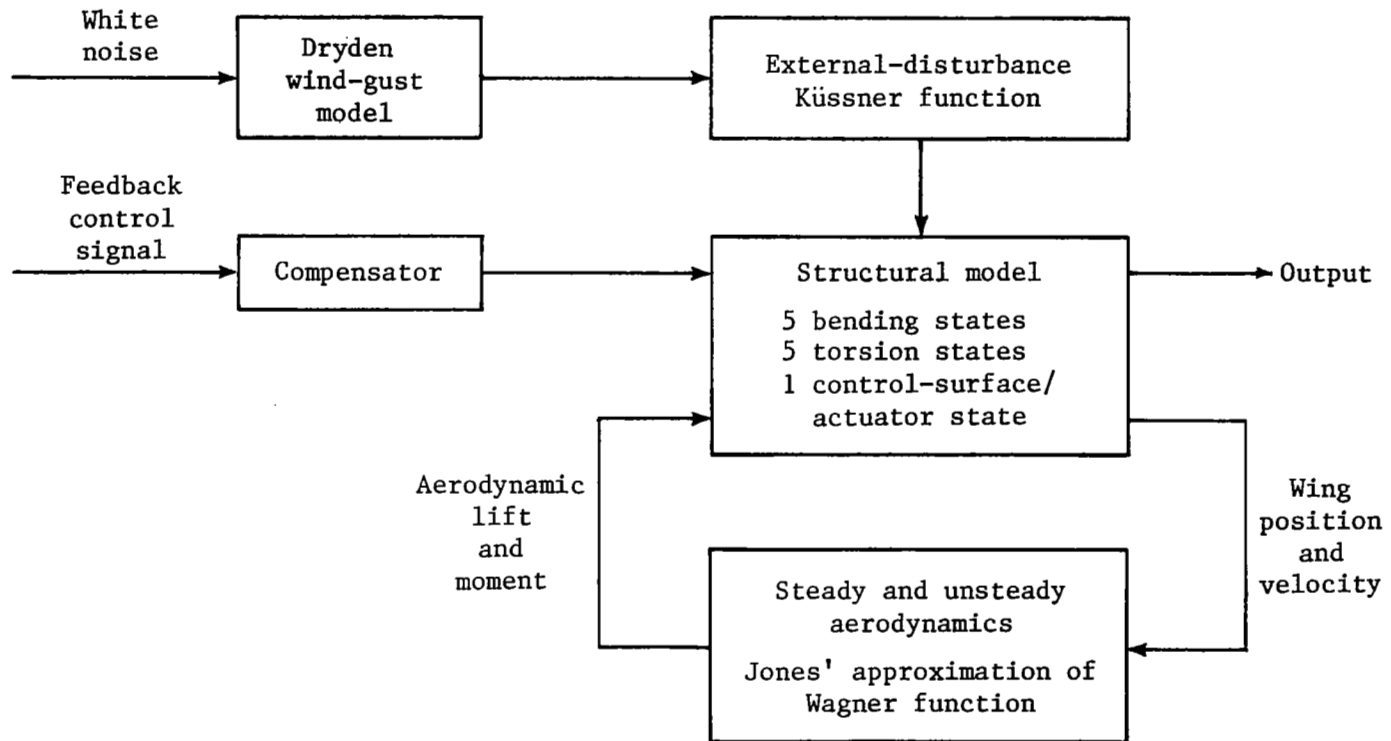


Figure 2.- Block diagram of open-loop-system model.

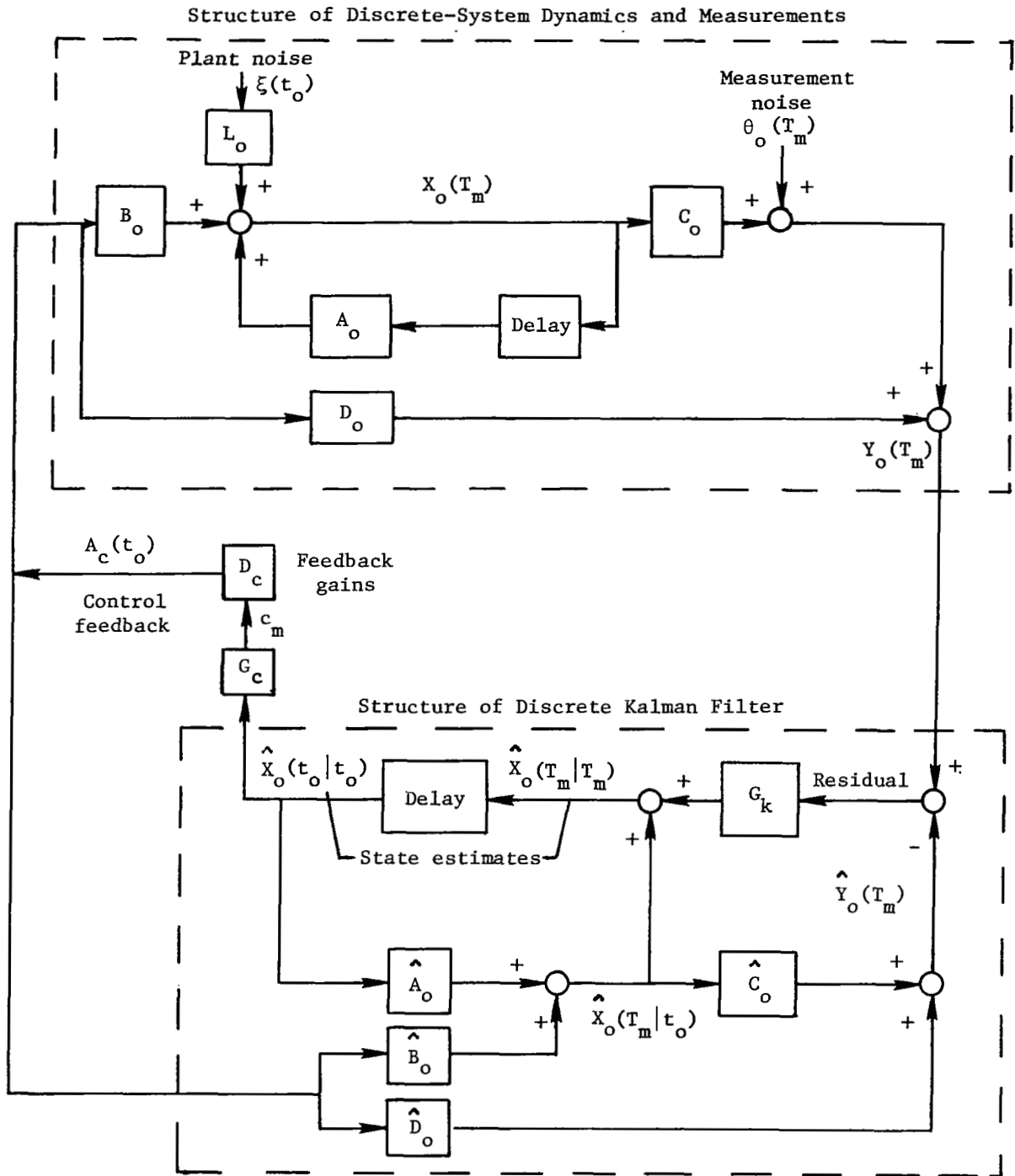


Figure 3.- Total discrete-system structure.

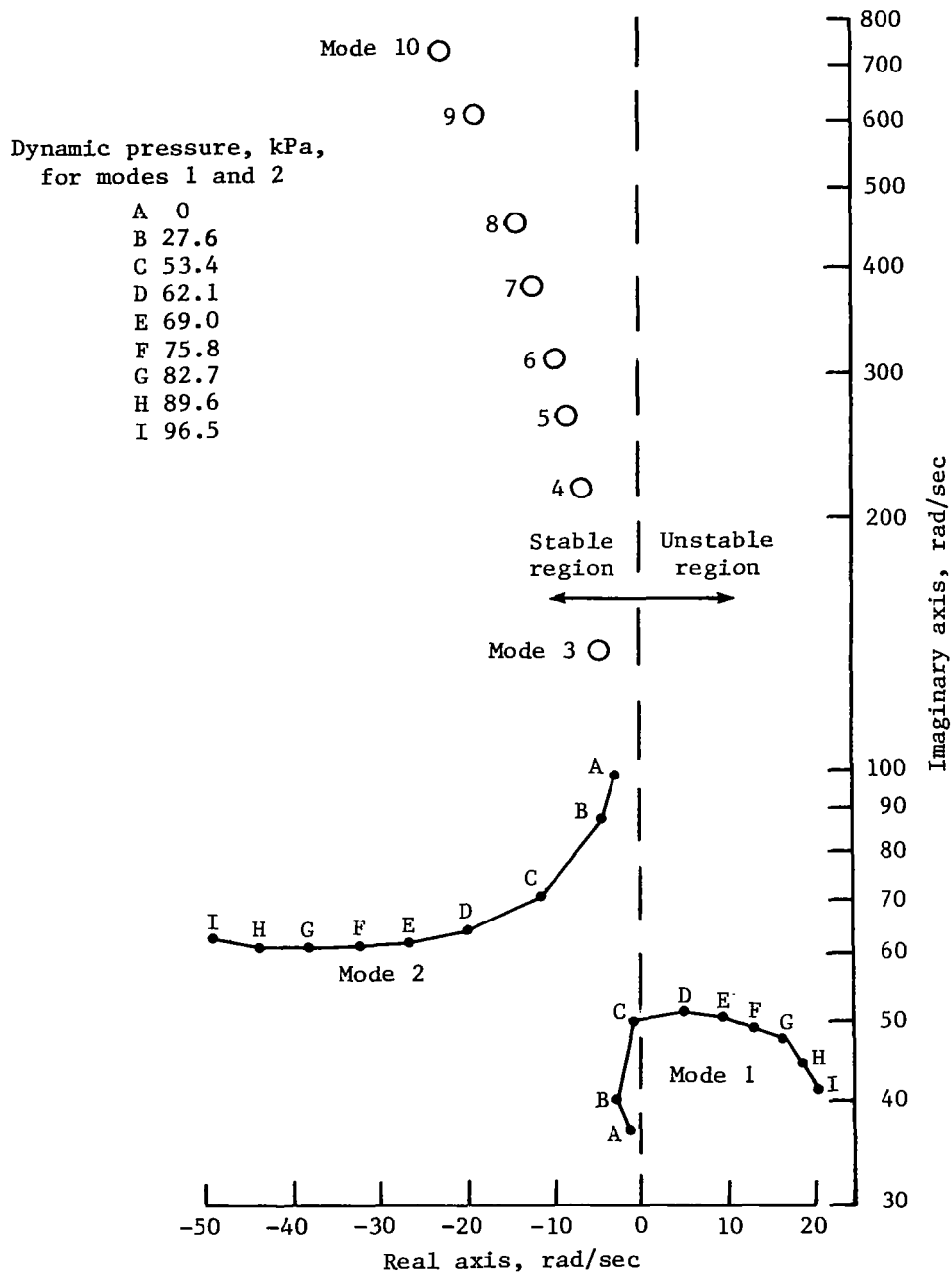


Figure 4.- Flexible-wing modes as a function of dynamic pressure.

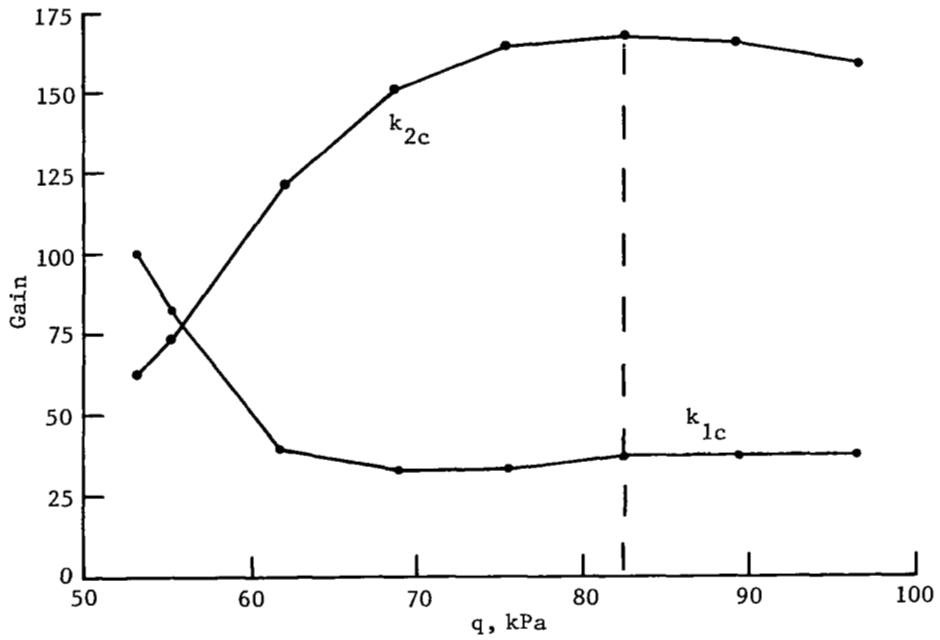


Figure 5.- Feedback gains to maintain design eigenvalue at $0.89 \pm 0.33j$ for all q . (Dashed line indicates constant q of 82.7 kPa.)

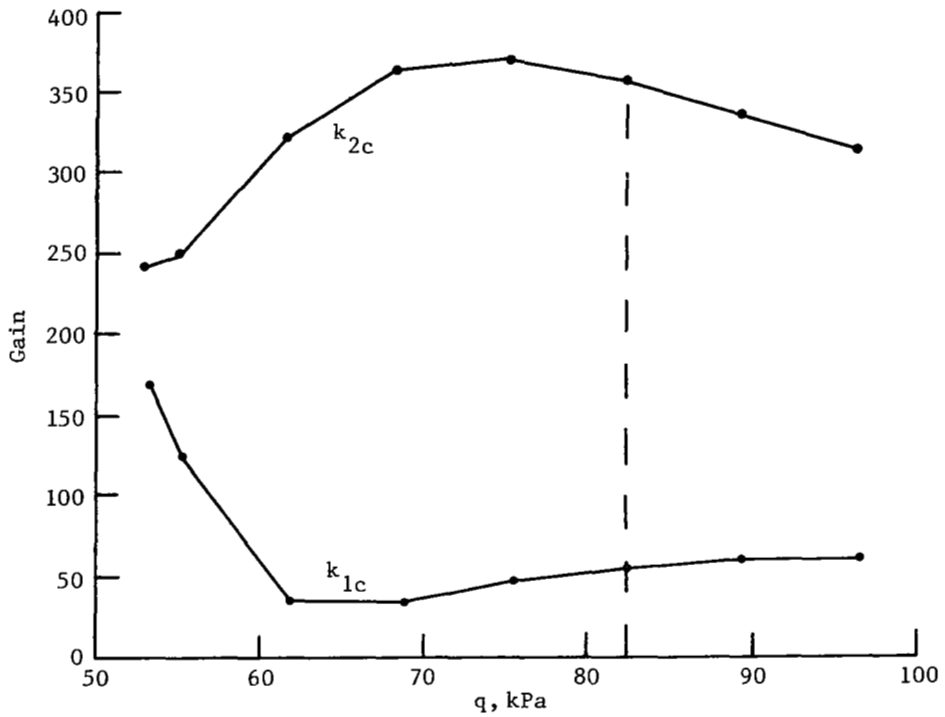


Figure 6.- Feedback gains to maintain design eigenvalue at $0.70 \pm 0.27j$ for all q . (Dashed line indicates constant q of 82.7 kPa.)

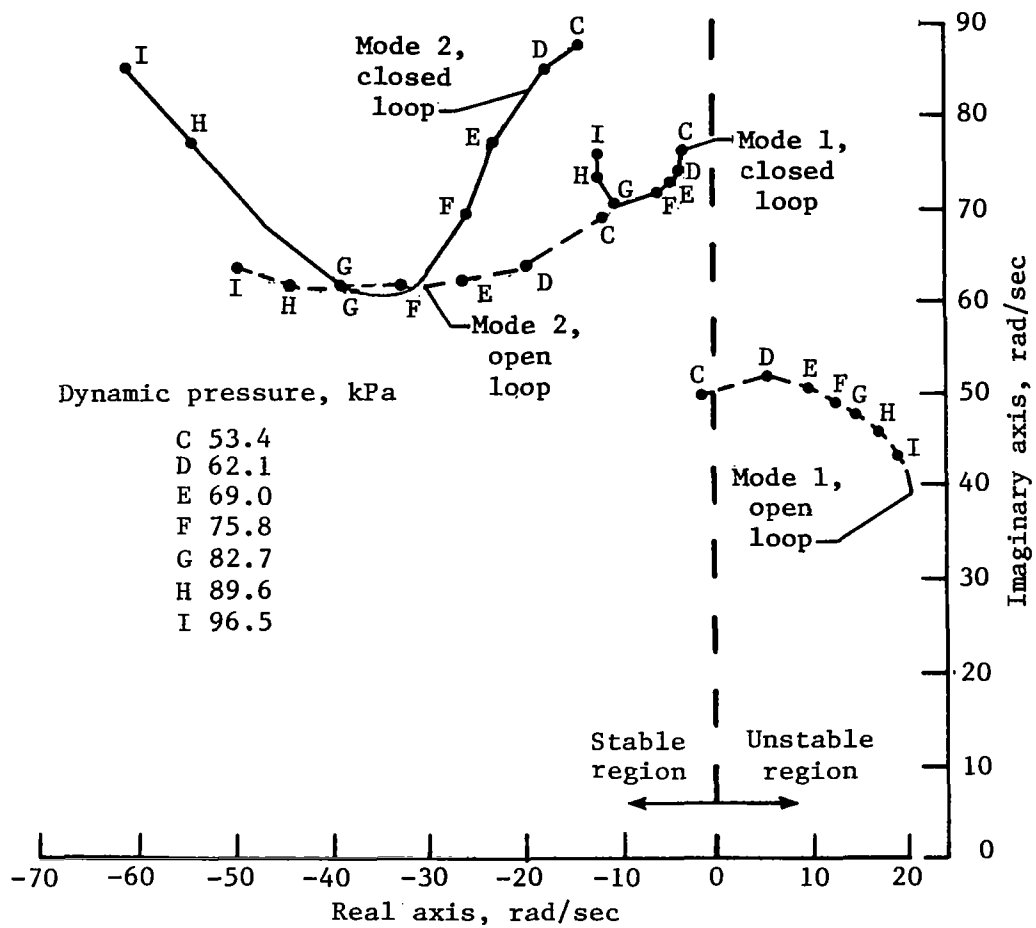


Figure 7.- Eigenvalue variations of first two modes as function of dynamic pressure for case of full-state estimation with mode 1 closed-loop design eigenvalue at $0.89 \pm 0.33j$ ($s = -10 \pm 70j$) for $q = 82.7$ kPa.

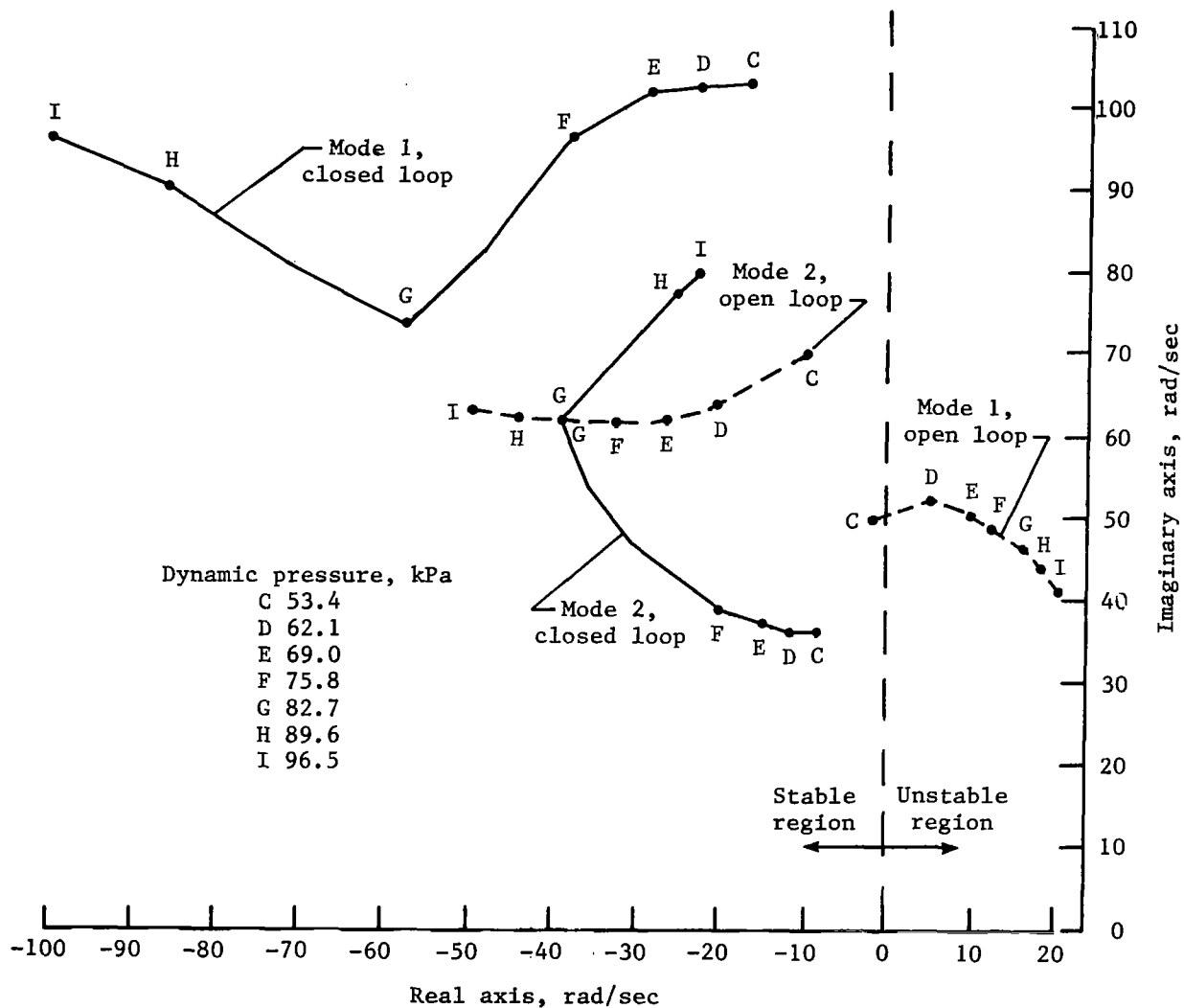


Figure 8.- Eigenvalue variations of first two modes as a function of dynamic pressure for case of full-state estimation with mode 1 closed-loop design eigenvalue at $0.7 \pm 0.27j$ ($s = -58 \pm 74j$) for $q = 82.7$ kPa.

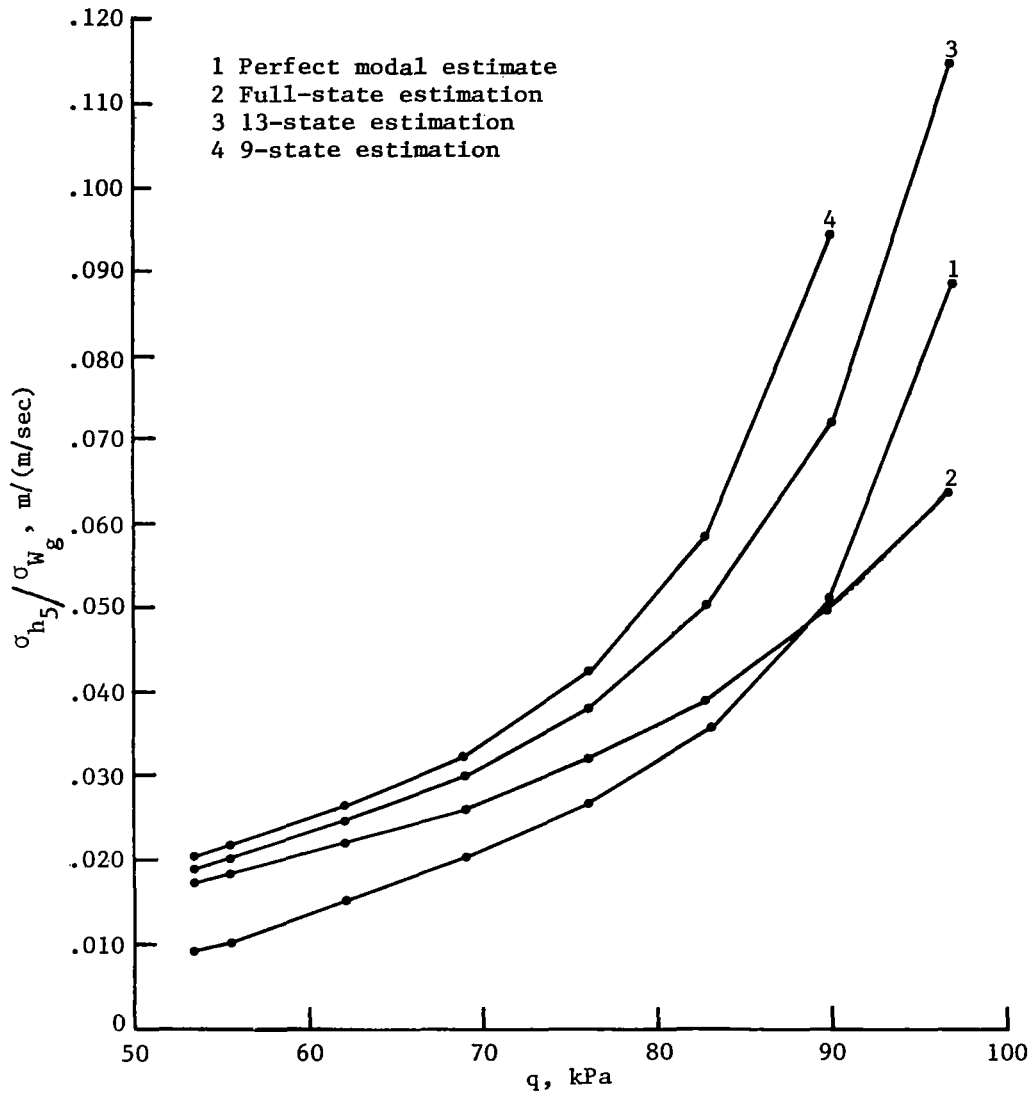


Figure 9.- Root-mean-square wing-tip bending for 1 m/sec rms wind gust as a function of dynamic pressure for design eigenvalue of $0.89 \pm 0.33j$ ($s = -10 \pm 70j$).

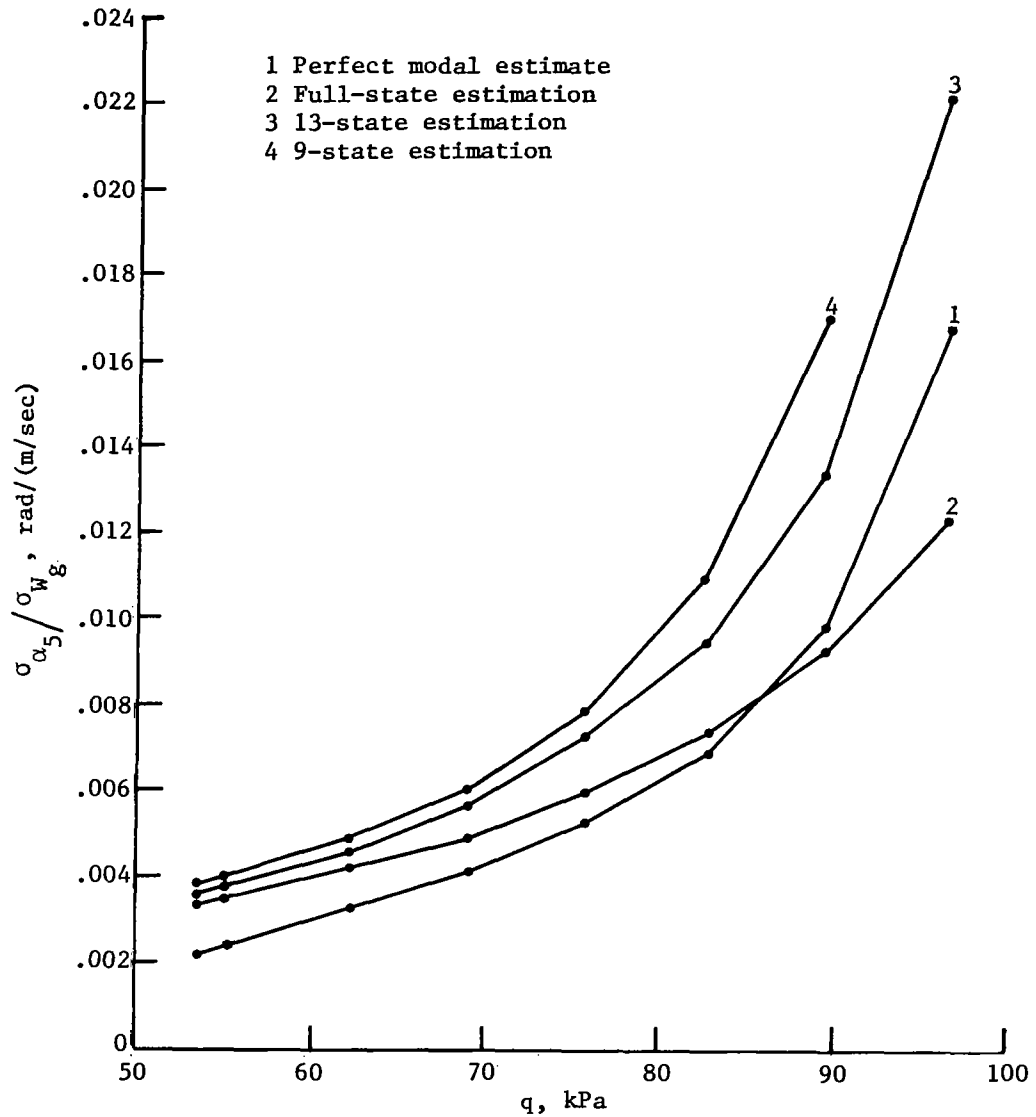


Figure 10.- Root-mean-square wing-tip rotation for 1 m/sec rms wind gust as a function of dynamic pressure for design eigenvalue of $0.89 \pm 0.33j$ ($s = -10 \pm 70j$).

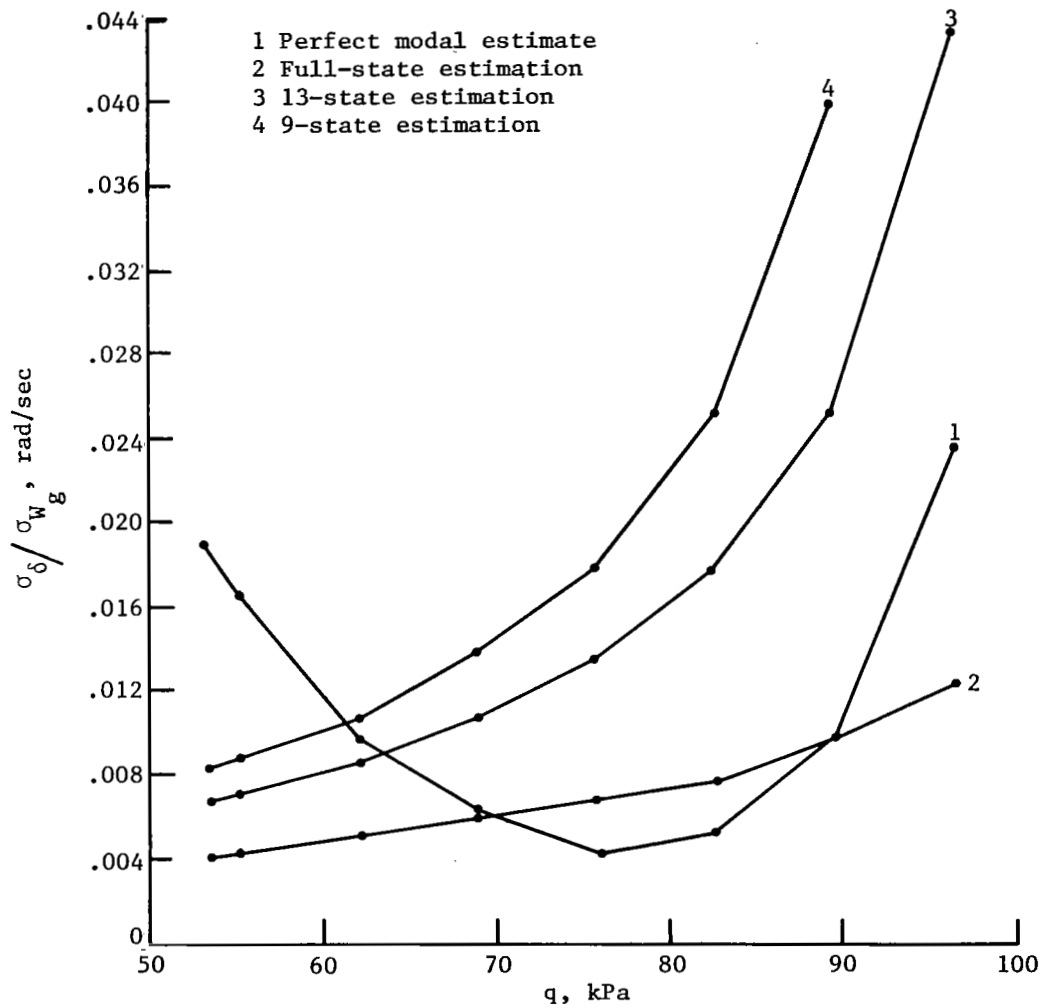


Figure 11.- Root-mean-square control-surface rotation for 1 m/sec rms wind gust as a function of dynamic pressure for design eigenvalues of $0.89 \pm 0.33j$ ($s = -10 \pm 70j$).

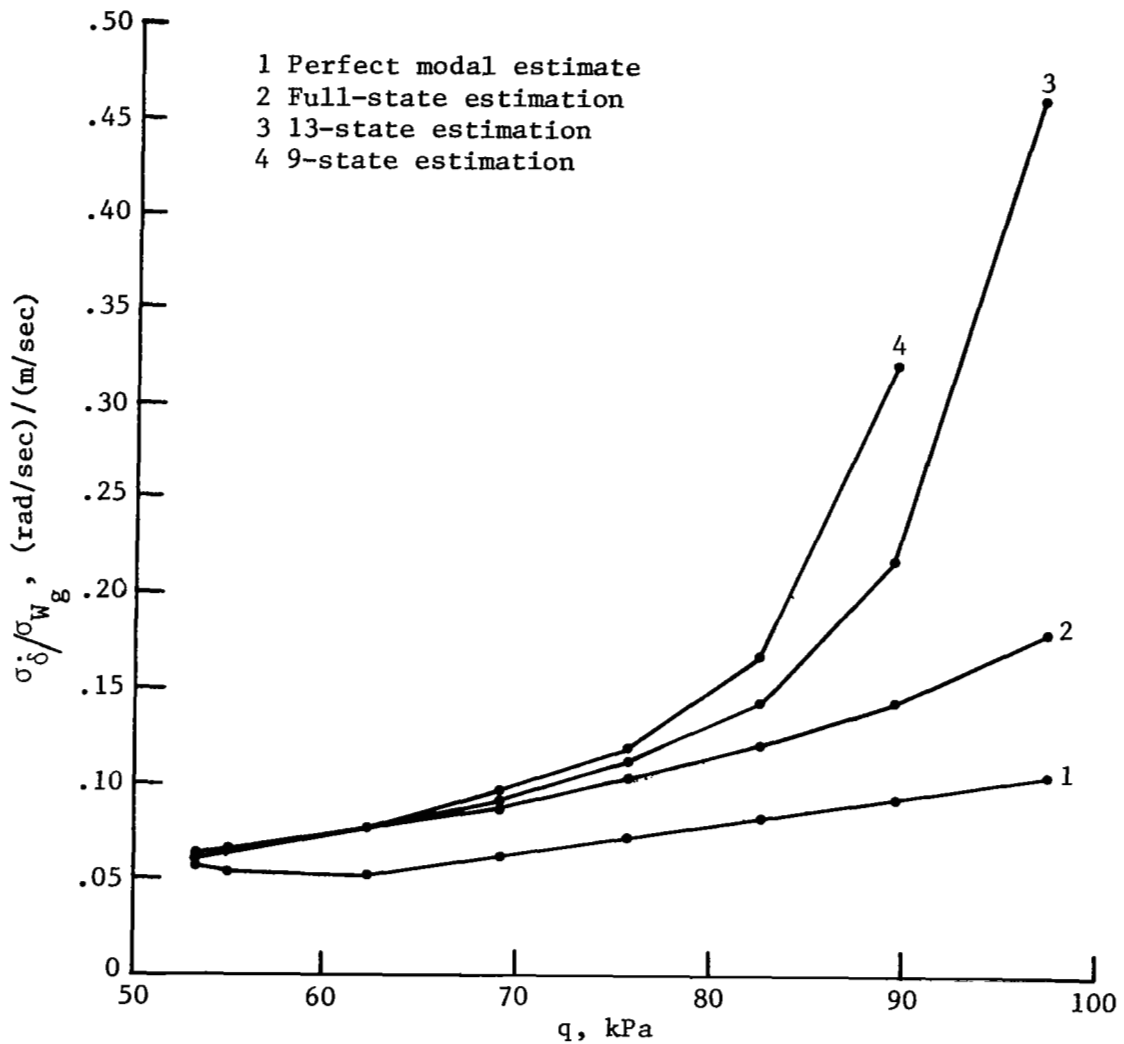


Figure 12.- Root-mean-square control-surface velocity for 1 m/sec rms wind gust as a function of dynamic pressure for design eigenvalue of $0.89 \pm 0.33j$ ($s = -10 \pm 70j$).

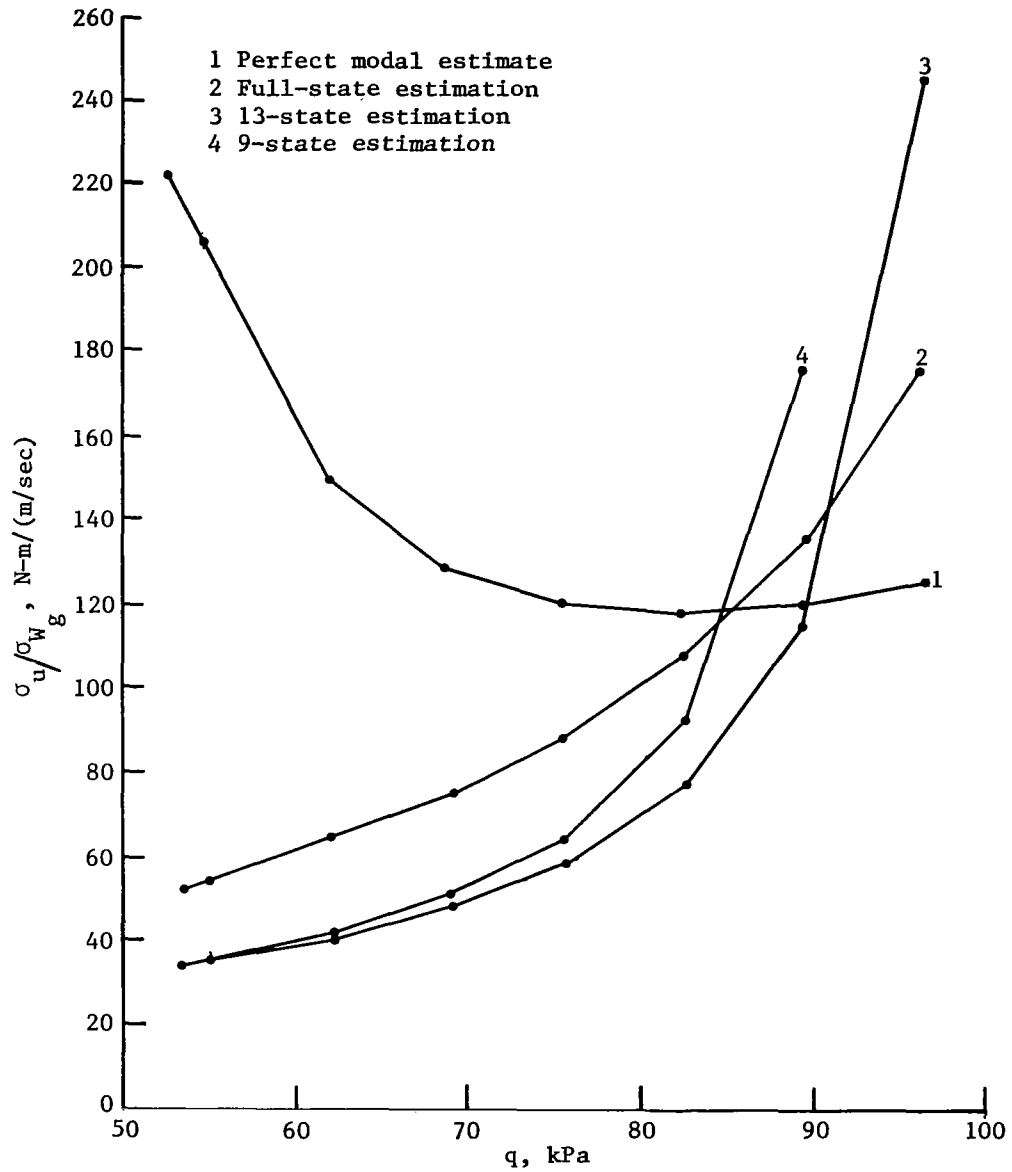


Figure 13.- Root-mean-square control-torque input command for 1 m/sec rms wind gust as a function of dynamic pressure for design eigenvalue of $0.89 \pm 0.33j$ ($s = -10 \pm 70j$).

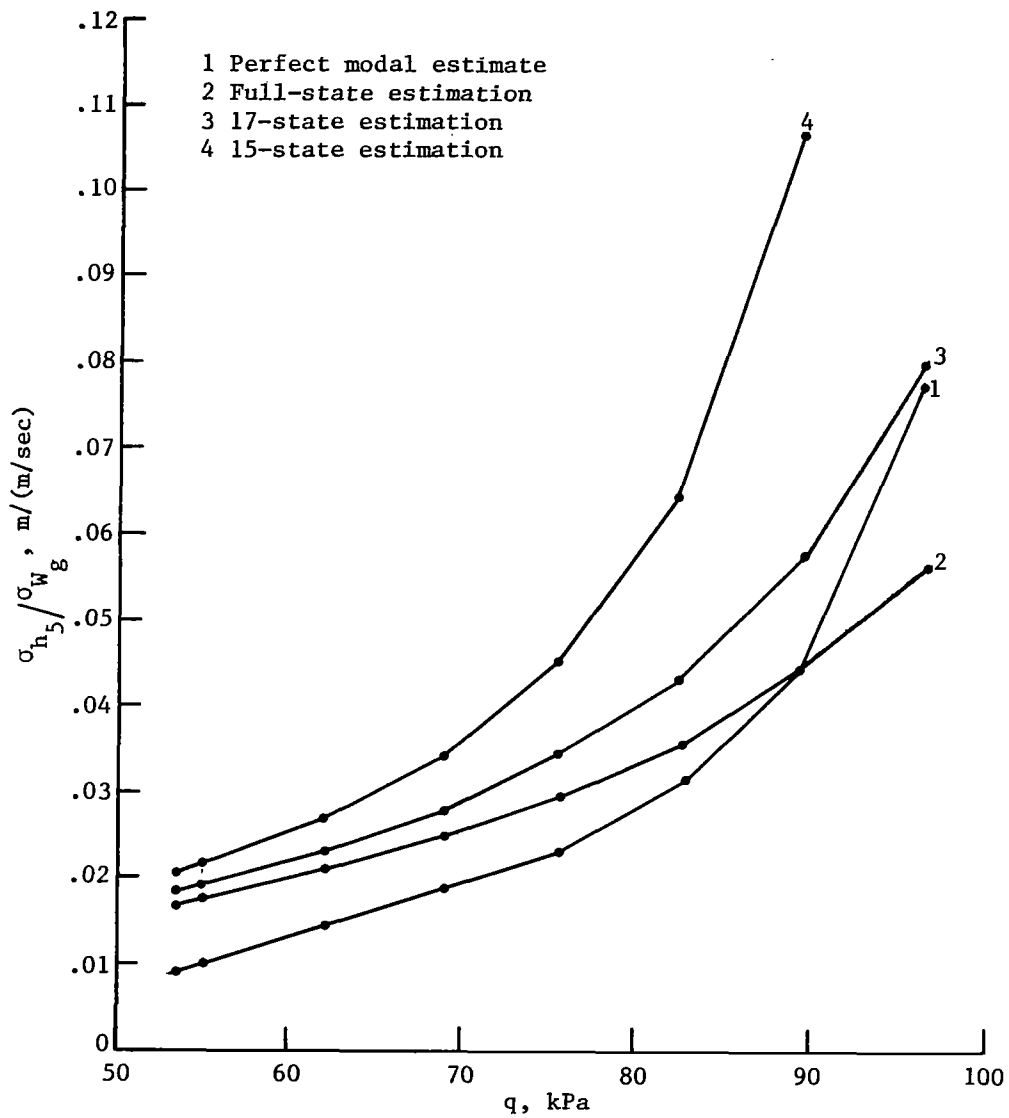


Figure 14.- Root-mean-square wing-tip bending for 1 m/sec rms wind gust as a function of dynamic pressure for design eigenvalue of $0.70 \pm 0.27j$ ($s = -58 \pm 74j$).

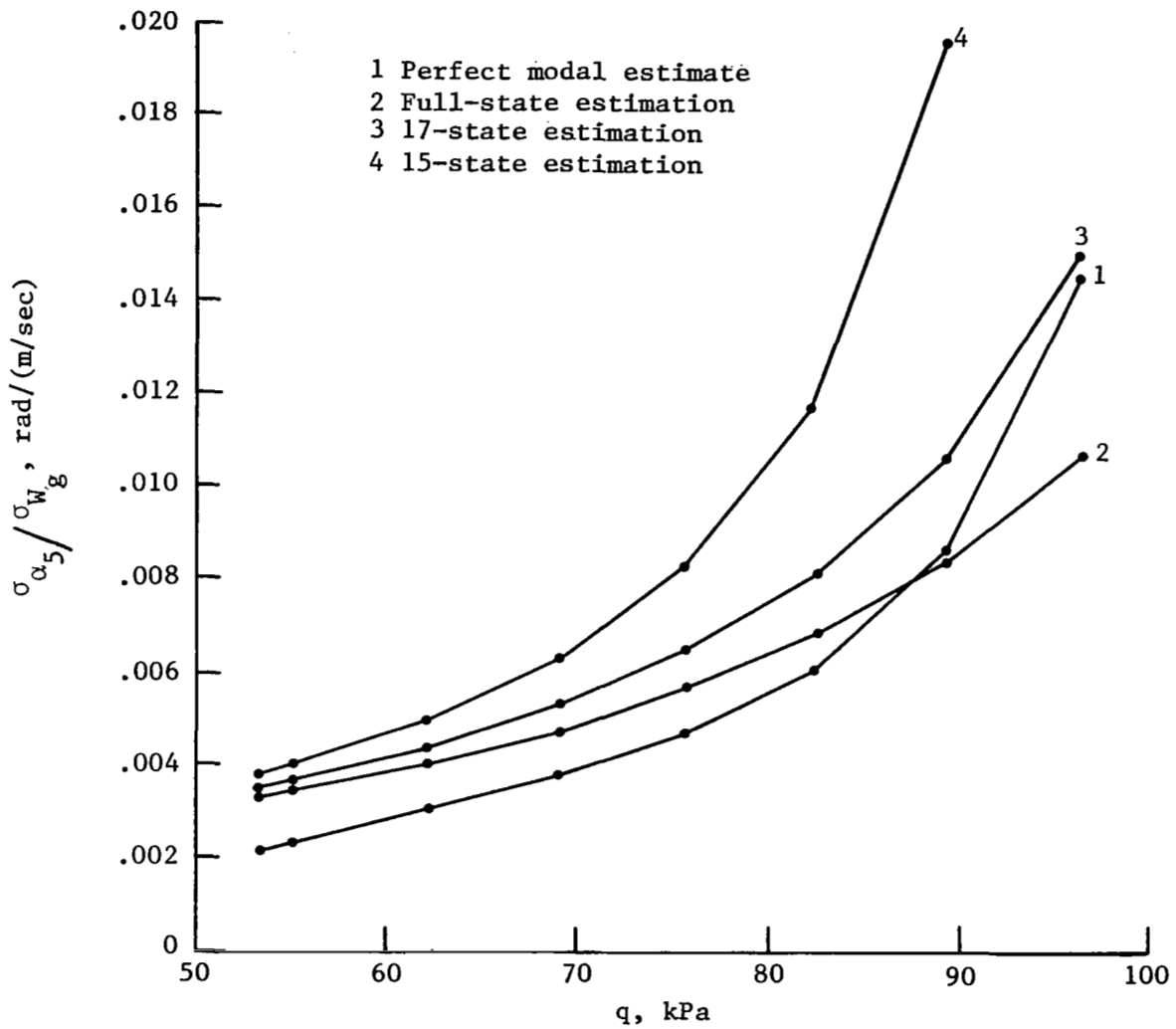


Figure 15.- Root-mean-square wing-tip rotation for 1 m/sec rms wind gust as a function of dynamic pressure for design eigenvalue of $0.70 \pm 0.27j$ ($s = -58 \pm 74j$).

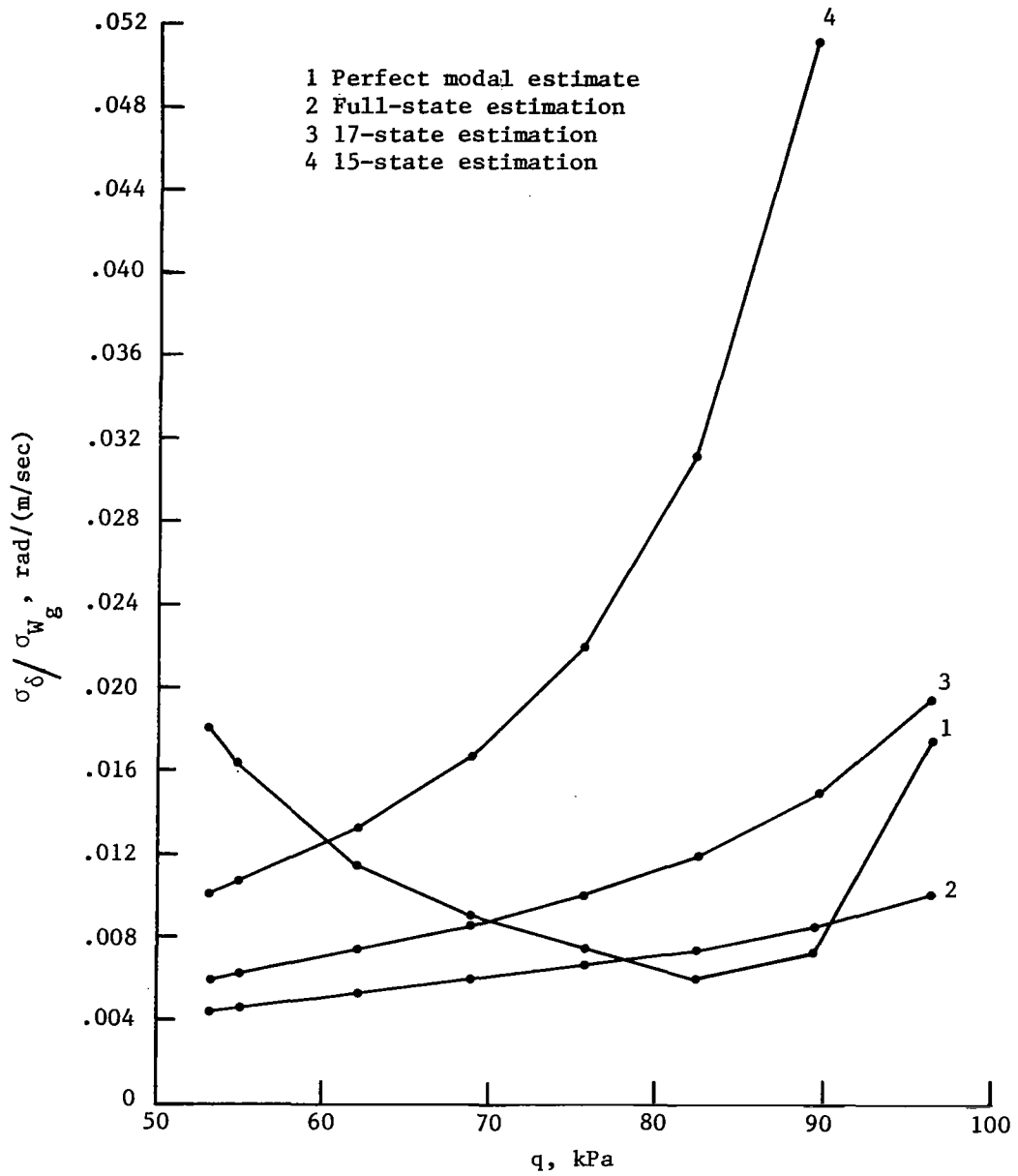


Figure 16.- Root-mean-square control-surface rotation for 1 m/sec rms wind gust as a function of dynamic pressure for design eigenvalue of $0.70 \pm 0.27j$ ($s = -58 \pm 74j$).

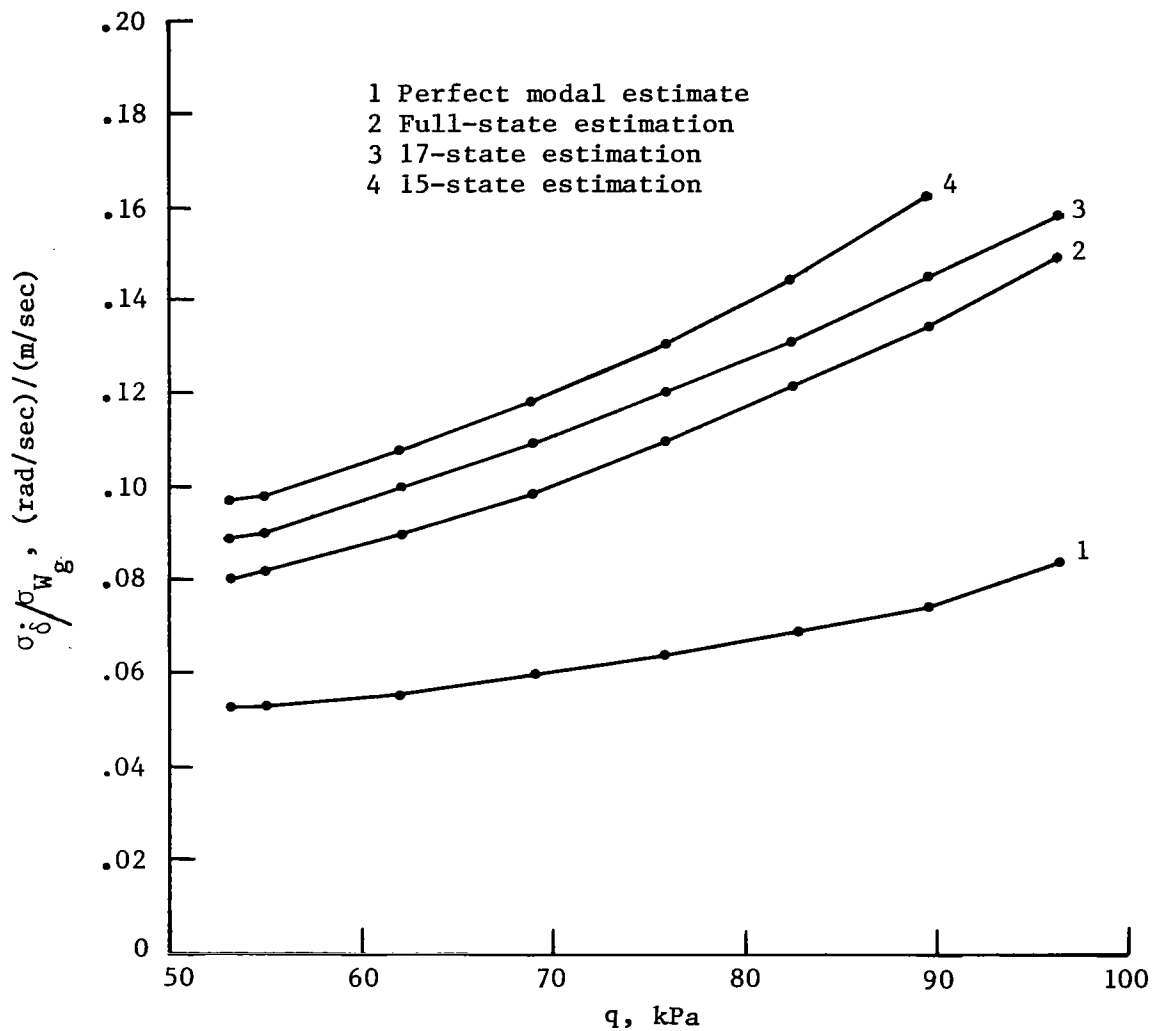


Figure 17.- Root-mean-square control-surface velocity for 1 m/sec rms wind gust as a function of dynamic pressure for design eigenvalue of $0.70 \pm 0.27j$ ($s = -58 \pm 74j$).

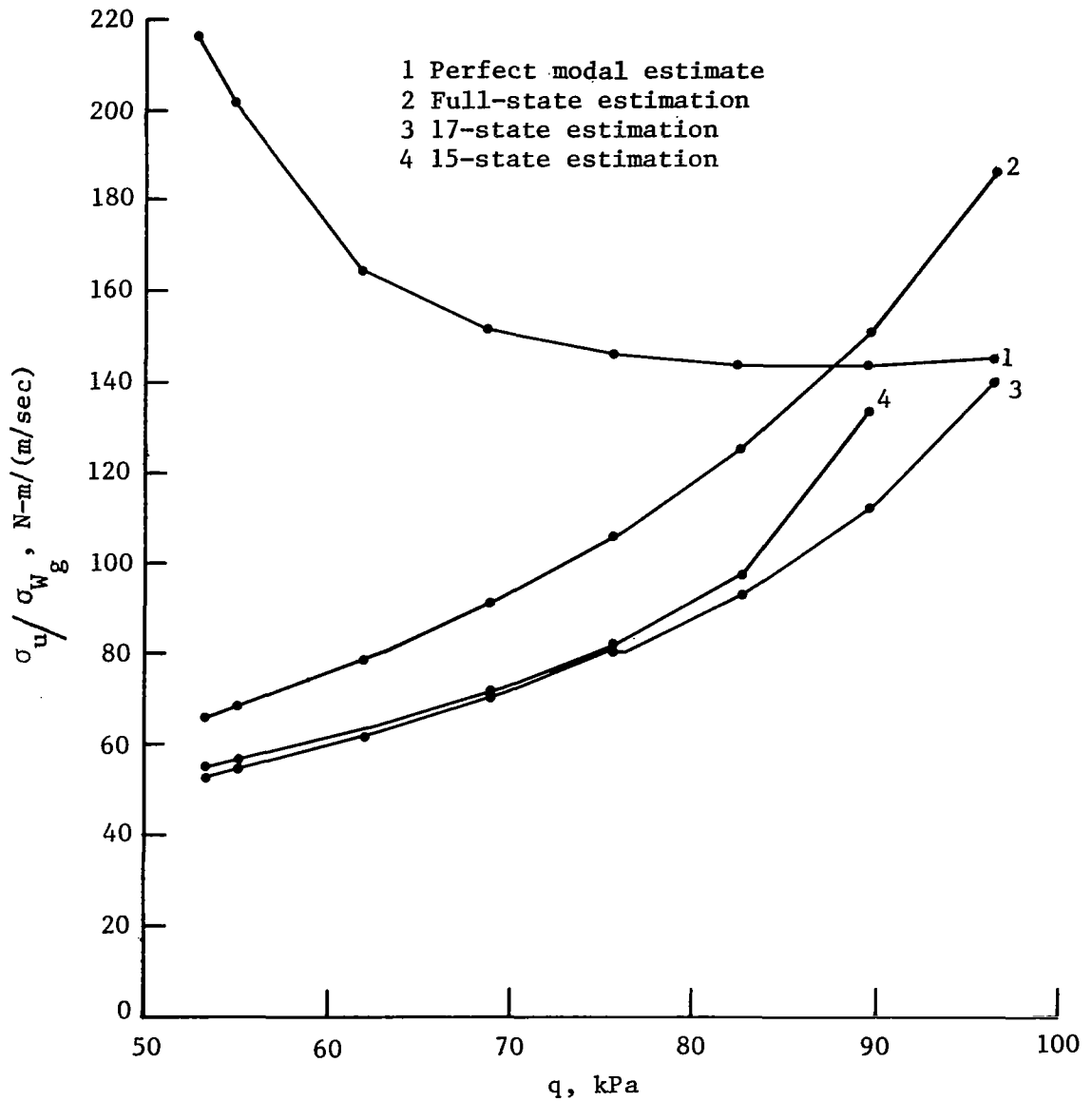


Figure 18.- Root-mean-square control-torque input command for 1 m/sec rms wind gust as a function of dynamic pressure for design eigenvalue of $0.70 \pm 0.27j$ ($s = -58 \pm 74j$).

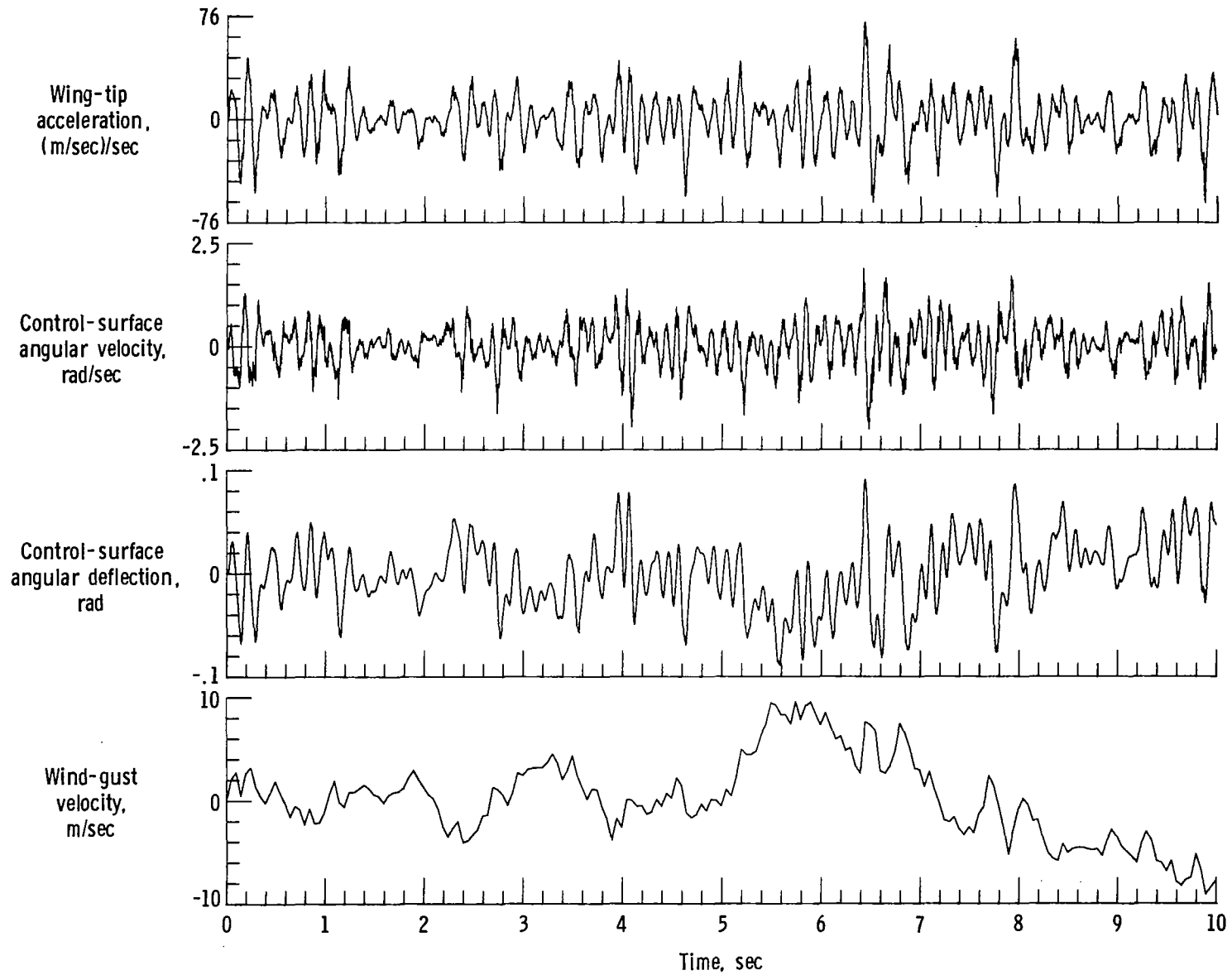


Figure 19.- Typical signals for full-state estimation case. $q = 82.7$ kPa; design eigenvalue is $0.89 \pm 0.33j$ with random and bias measurement errors.

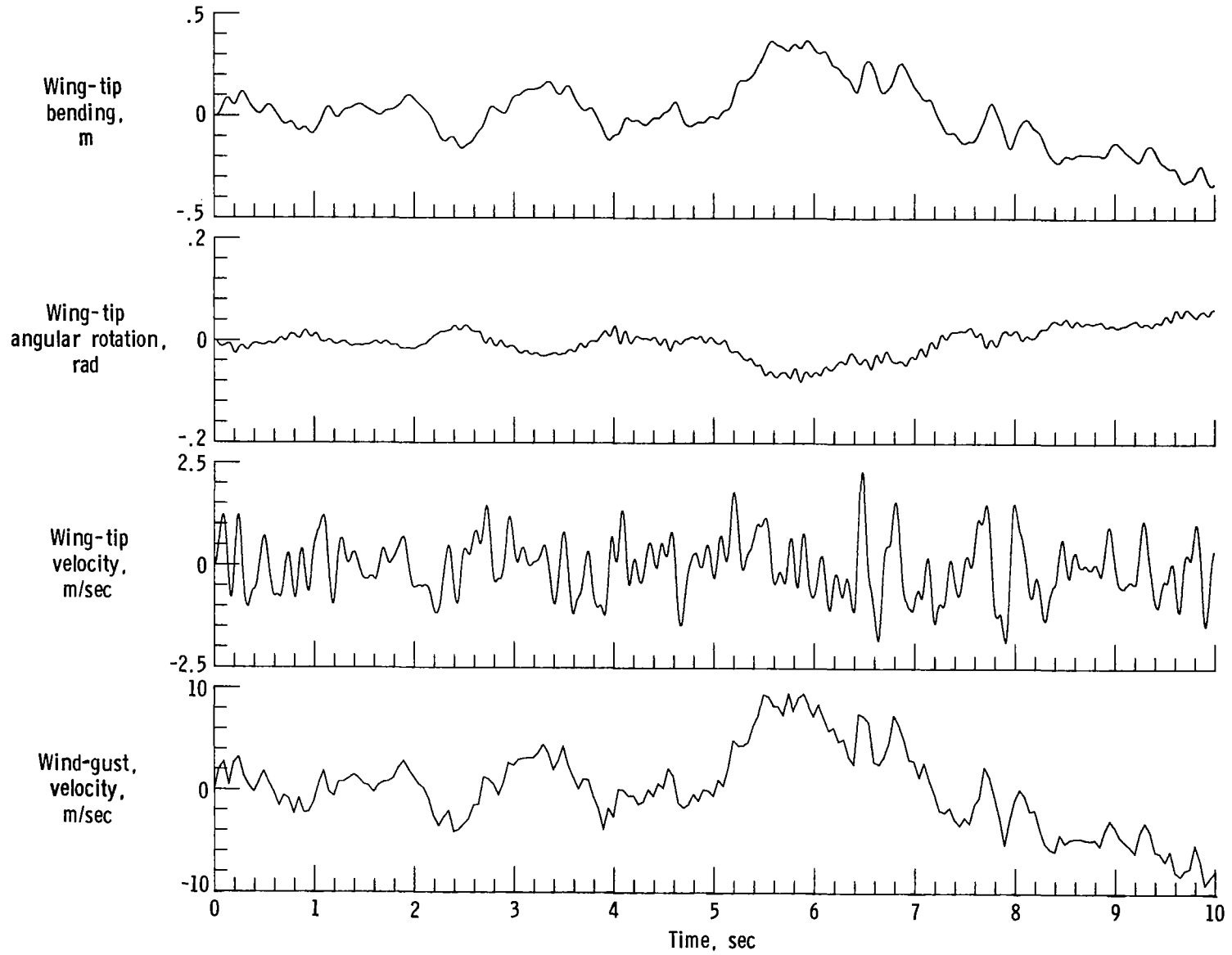


Figure 19.- Continued.

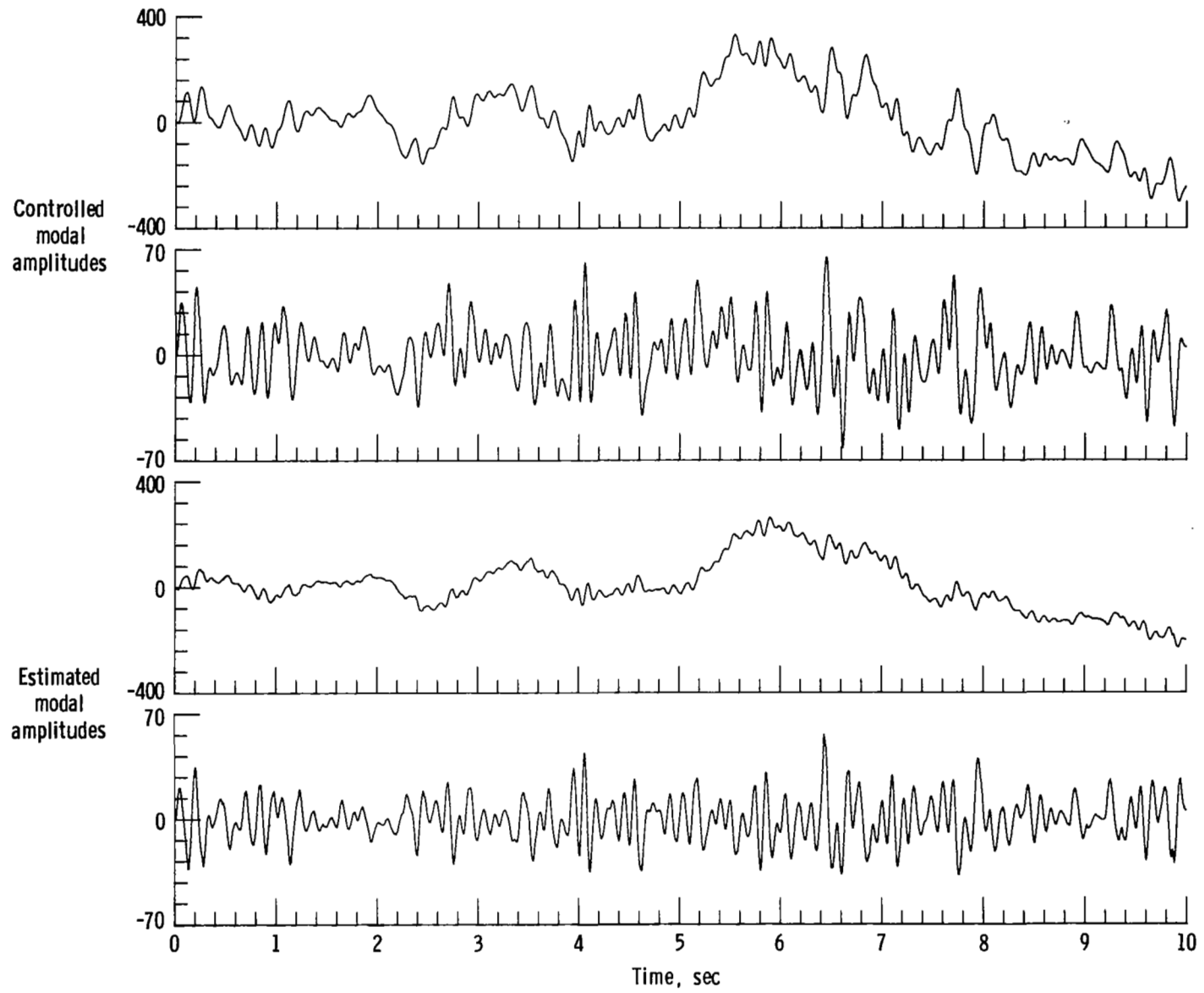
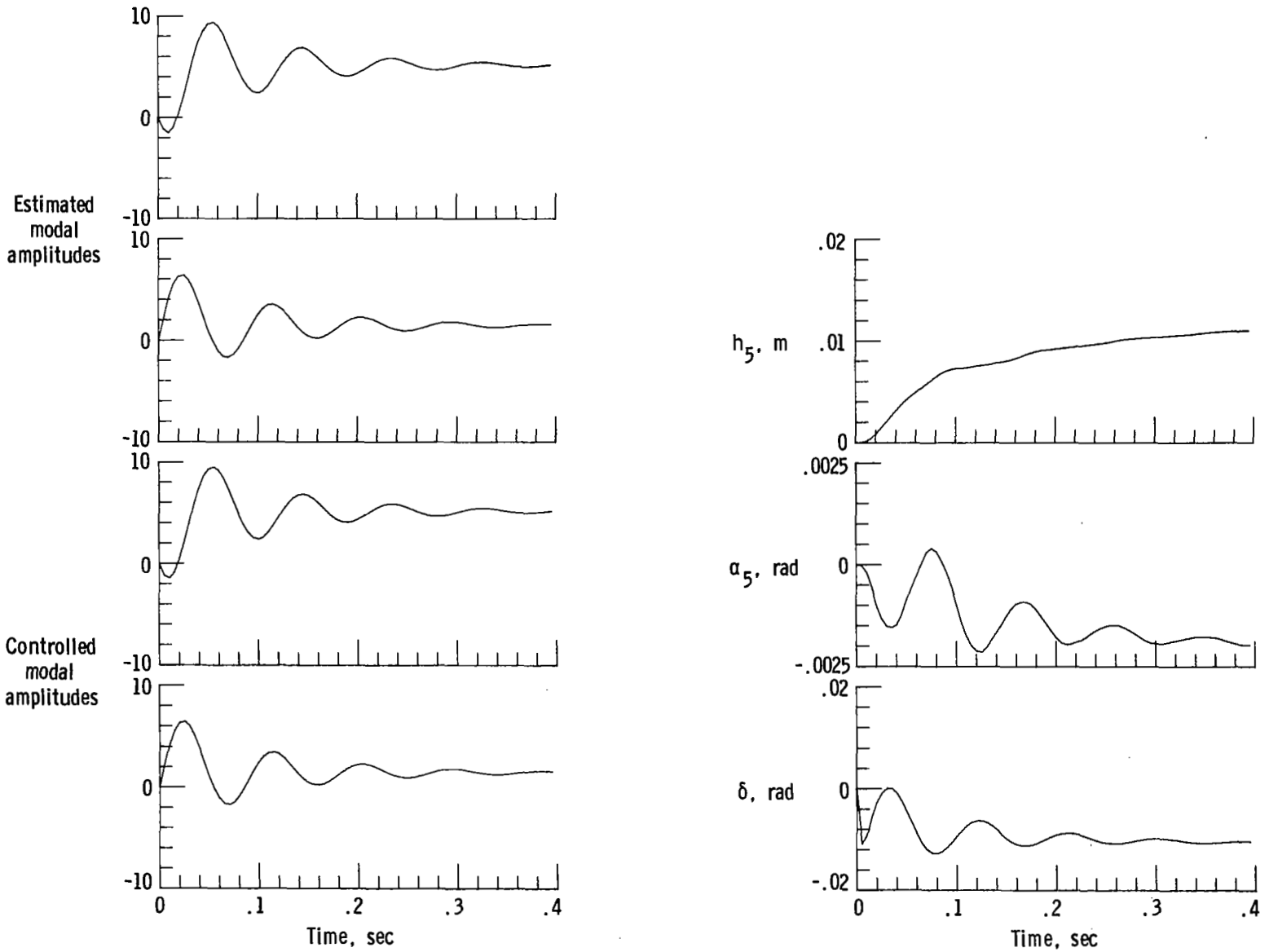
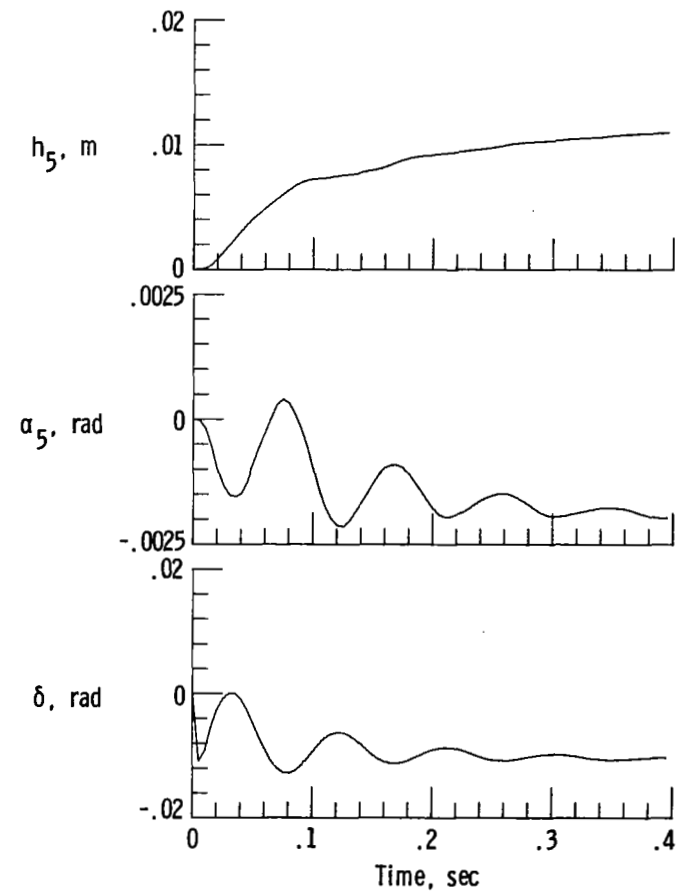
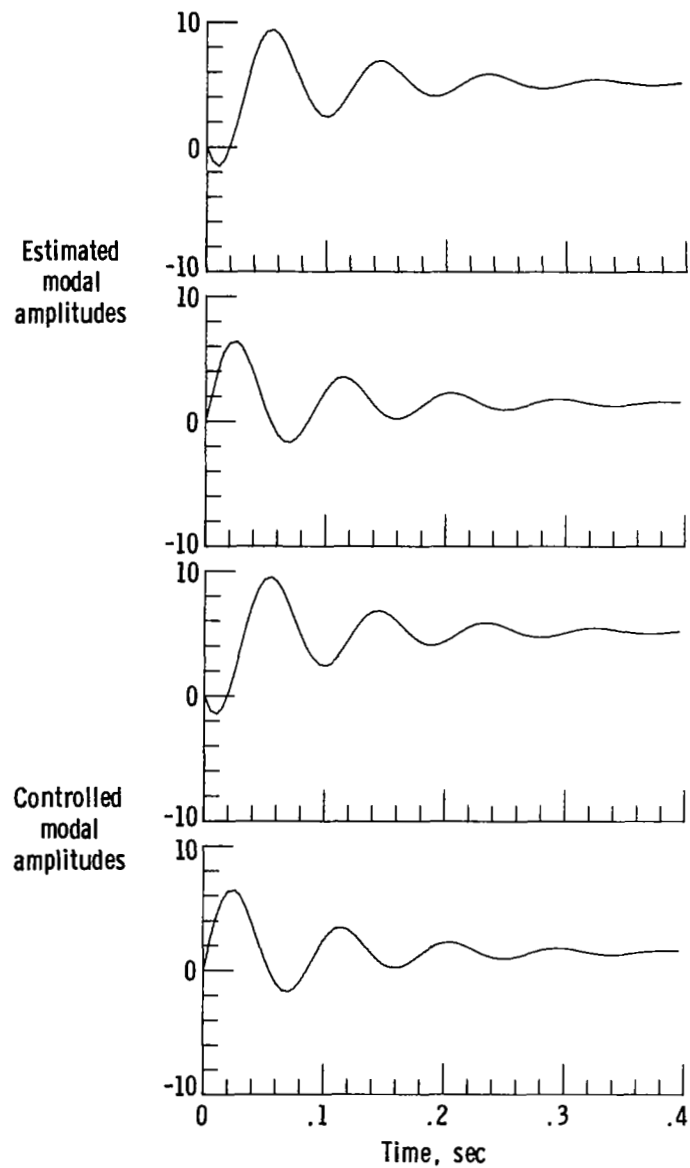


Figure 19.- Concluded.



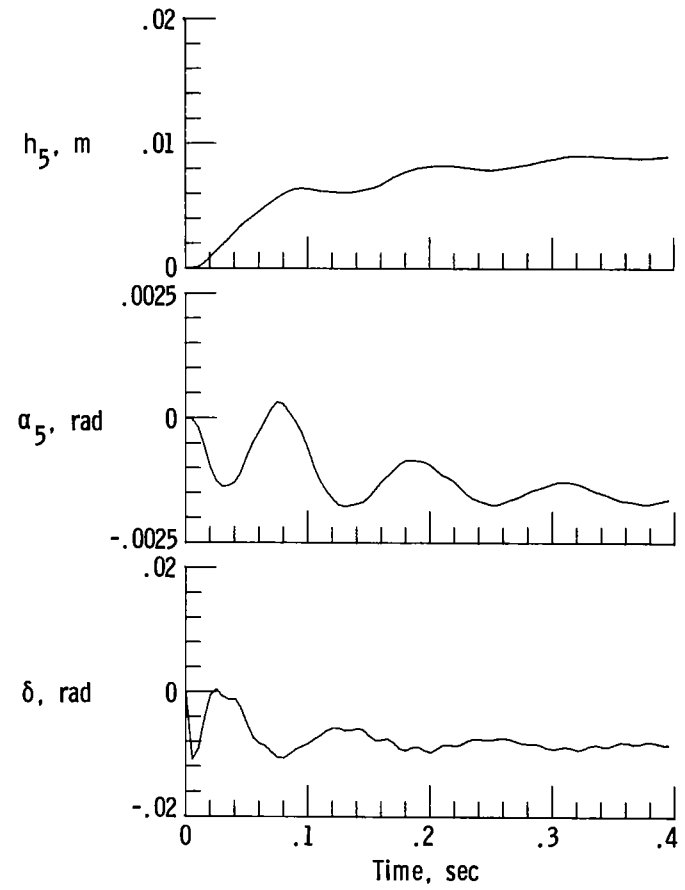
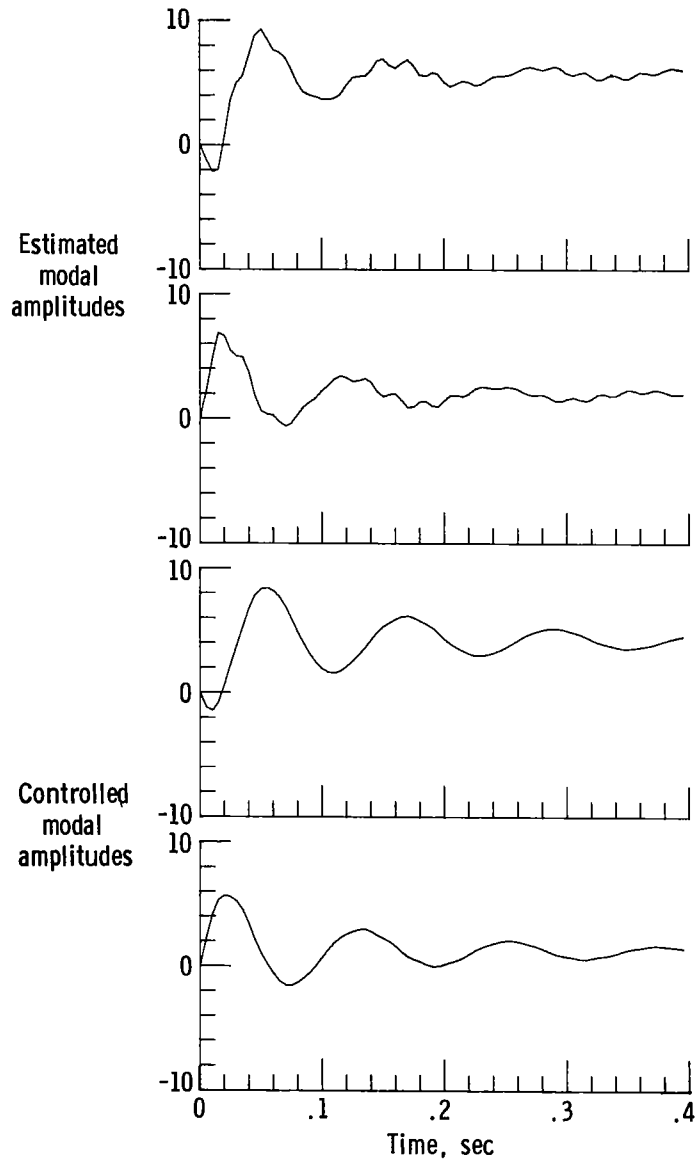
(a) Perfect modal estimation.

Figure 20.- Step responses resulting from external command at input of A_C .
 $q = 82.7 \text{ kPa}$; Design eigenvalue = $0.89 \pm 0.33j$.



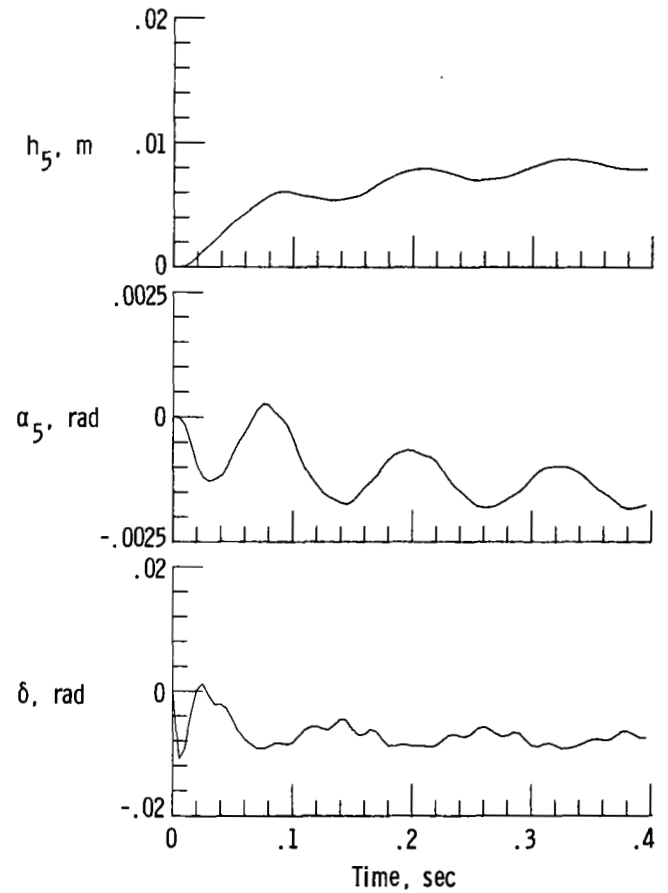
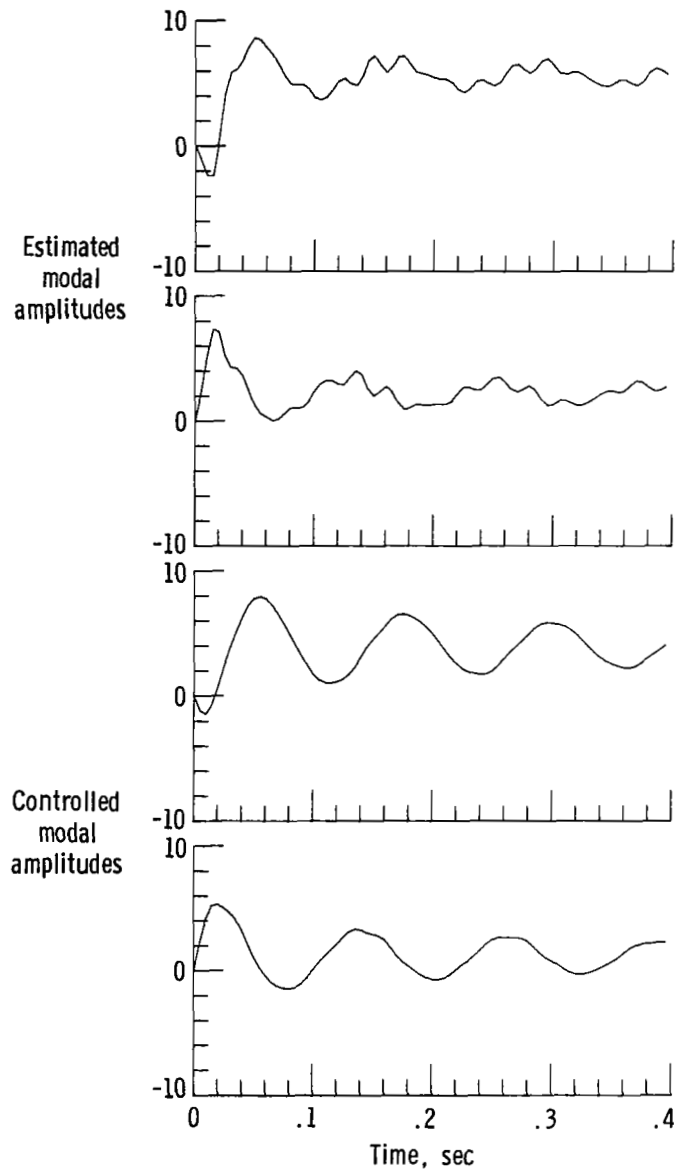
(b) Full-state estimation.

Figure 20.- Continued.



(c) Thirteen-state estimation.

Figure 20.- Continued.



(d) Nine-state estimation.

Figure 20.- Concluded.

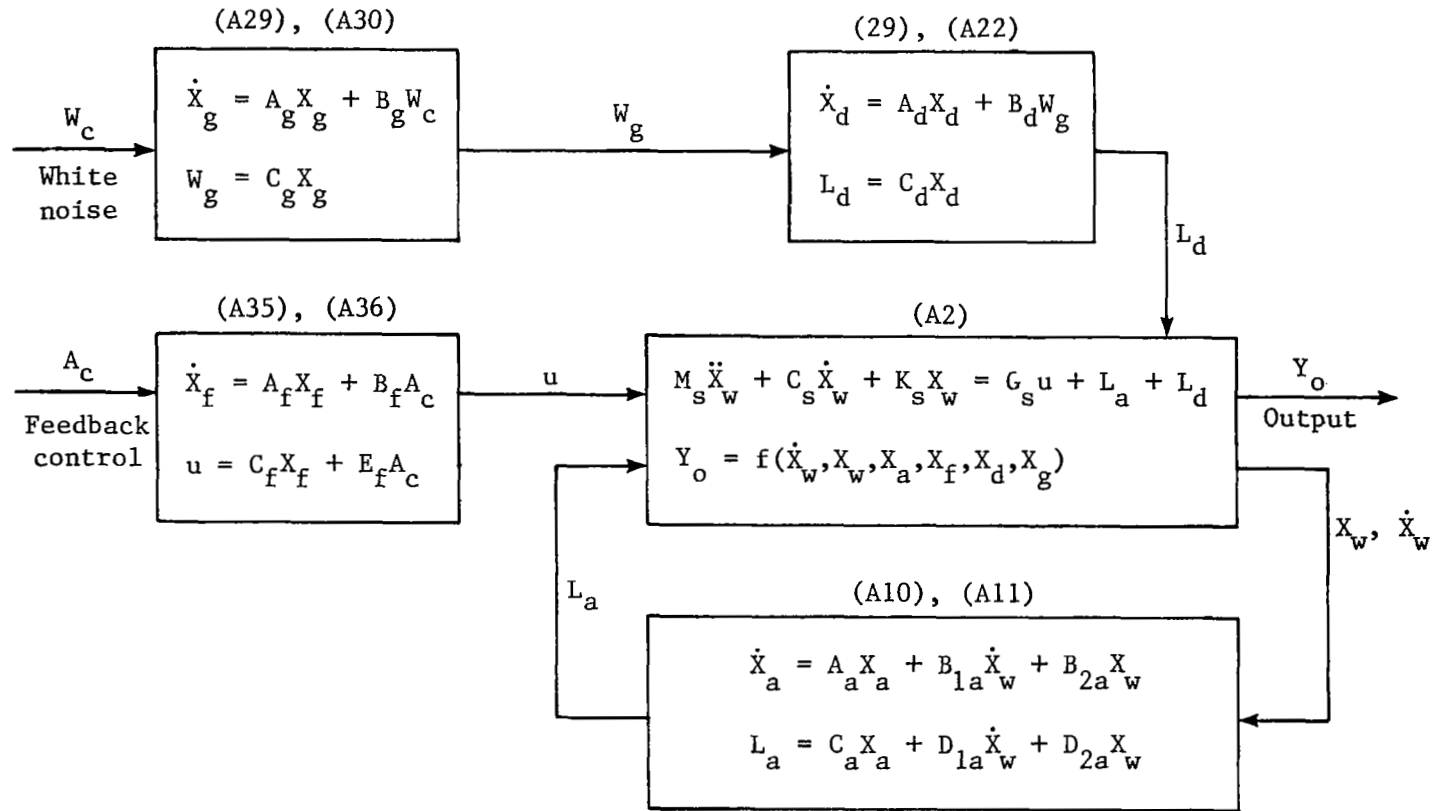


Figure 21.- Block diagram of open-loop-system model.

1. Report No. NASA TP-1983		2. Government Accession No.		3. Recipient's Catalog No.	
4. Title and Subtitle APPLICATION OF MODAL CONTROL TO WING-FLUTTER SUPPRESSION				5. Report Date May 1982	
				6. Performing Organization Code 505-34-33	
7. Author(s) Aaron J. Ostroff and Samuel Pines				8. Performing Organization Report No. L-14976	
9. Performing Organization Name and Address NASA Langley Research Center Hampton, VA 23665				10. Work Unit No.	
				11. Contract or Grant No.	
12. Sponsoring Agency Name and Address National Aeronautics and Space Administration Washington, DC 20546				13. Type of Report and Period Covered Technical Paper	
				14. Sponsoring Agency Code	
15. Supplementary Notes Aaron J. Ostroff: Langley Research Center. Samuel Pines: Analytical Mechanics Associates, Inc., Jericho, New York.					
16. Abstract This paper describes a discrete modal control design approach that is applied to a single-control-surface, unswept aircraft wing subject to bending-torsion flutter. The modal approach is a mathematical method to decouple the equations of motion into isolated differential equations. In this paper, a pole-placement approach is then applied to determine stability gains in the discrete plane using only the two complex-conjugate flutter-mode equations. A fixed-gain Kalman filter is used to estimate the modal amplitudes using three measurements. Results are presented for a full-state estimator (36 states) and two reduced-state estimators using two different closed-loop pole locations. The control law is designed for a dynamic pressure that is 50 percent greater than the uncontrolled-flutter dynamic pressure. With constant control-law gains, the closed-loop system remains stable over the dynamic-pressure range from flutter onset to approximately an 80-percent increase in pressure.					
17. Key Words (Suggested by Author(s)) Flutter suppression Modal control Discrete control Aeroelasticity			18. Distribution Statement Unclassified - Unlimited Subject Category 08		
19. Security Classif. (of this report) Unclassified	20. Security Classif. (of this page) Unclassified	21. No. of Pages 71	22. Price A04		

National Aeronautics and
Space Administration

THIRD-CLASS BULK RATE

Postage and Fees Paid
National Aeronautics and
Space Administration
NASA-451



Washington, D.C.
20546

Official Business
Penalty

2 1 1J, A, 820507 50000305
DEPT OF THE AIR FORCE
AF WEAPONS LABORATORY
ATTN: TECHNICAL LIBRARY (SUL)
KIRTLAND AFB NM 87117

NASA

POSTMASTER: If Undeliverable (Section 158
Postal Manual) Do Not Return